Microseismic investigation of an unstable mountain slope in the Swiss Alps

Thomas Spillmann,[1,2] Hansruedi Maurer,[1] Alan G. Green,[1] Björn Heincke,[1,3] Heike Willenberg,[4] and Stephan Husen[5]

Received 24 August 2006; revised 22 January 2007; accepted 19 February 2007; published 4 July 2007.

[1] Risks associated with unstable rocky slopes are growing as a result of climate change and rapid expansions of human habitats and critical infrastructure in mountainous regions. To improve our understanding of mountain slope instability, we developed a microseismic monitoring system that operates autonomously in remote areas afflicted by harsh weather. Our microseismic system comprising 12 three-component geophones was deployed across $\sim$60,000 m^2 of rugged crystalline terrain above a huge (30 million m^3) recent rockfall in the Swiss Alps. During its 31-month lifetime, signals from 223 microearthquakes with approximate moment magnitudes ranging from -2 to 0 were recorded. Determining the hypocenters was challenging for several reasons: (1) *P* wave velocities were highly heterogeneous, varying abruptly from <1.5 km/s to >3.8 km/s. (2) First-break picks were either inaccurate or lacking for some microearthquakes. (3) There were no reliable *S* wave picks. (4) Numerous microearthquakes occurred just outside the network boundaries. These issues were addressed by using a three-dimensional (3-D) *P* wave velocity model of the mountain slope determined from refraction tomography in a nonlinear inversion for hypocenter parameters and their probability density functions. Recordings from geophones at different altitudes and in boreholes constrained microearthquake depth estimates. Most microearthquakes were concentrated within 50–100 m of the surface in two zones, one that followed the recent rockslide scarp and one that spanned the volume of highest fracture zone/fault density. These two active zones delineated a mass of rock that according to geodetic measurements has moved toward the scarp at 1–2 cm/yr.

Citation: Spillmann, T., H. Maurer, A. G. Green, B. Heincke, H. Willenberg, and S. Husen (2007), Microseismic investigation of an unstable mountain slope in the Swiss Alps, *J. Geophys. Res.*, *112*, B07301, doi:10.1029/2006JB004723.

1. Introduction

[2] Risks associated with sudden mountain slope failures are escalating as a result of increases in exceptional climatic events and accelerated melting of alpine permafrost due to global warming and rapidly expanding population centers, lifelines (e.g., roads, railways, pipelines etc.), and other critical infrastructure within mountain valleys [*Glade et al.*, 2005; *Geertsema et al.*, 2006]. To mitigate the effects of mountain slope failures, robust protective barriers and early warning systems need to be constructed in the most vulnerable regions. Such installations require reliable information on the locations and key characteristics of unstable rock masses.

[3] Conventional strategies for identifying unstable mountain slopes and estimating the volumes, lithologies, and physical properties of susceptible rocks have involved geomorphological and geological mapping and geotechnical investigations [*Glade et al.*, 2005]. Relatively recently, various remote sensing techniques have allowed large mountainous areas to be rapidly examined [*Metternicht et al.*, 2005] and diverse geophysical methods have been used to investigate unstable and adjoining stable rock at depth [*McCann and Forster*, 1990; *Hack*, 2000]. As examples, geoelectrical, electromagnetic, seismic refraction, and surface wave surveys have supplied valuable information on the spatial variations of electrical resistivity and seismic velocity [*Bruno and Marillier*, 2000; *Cummings*, 2000; *Havenith et al.*, 2000; *Jongmans et al.*, 2000; *Mauritsch et al.*, 2000; *Schmutz et al.*, 2000; *Dussauge-Peisser et al.*, 2003; *Meric et al.*, 2005; *Brückl and Brückl*, 2006; *Godio et al.*, 2006; *Heincke et al.*, 2006b] and high-resolution seismic reflection and ground-penetrating radar (georadar or GPR) studies have yielded accurate subsurface images of active fractures and faults [*Bruno and Marillier*, 2000; *Dussauge-Peisser et al.*, 2003; *Heincke et al.*, 2005, 2006a; *Spillmann et al.*, 2007].

[4] Most of the above mentioned approaches only provide information on the static characteristics of the subsur-

[1]Institute of Geophysics, ETH-Zurich, Zurich, Switzerland.
[2]Now at Geothermal Explorers Ltd., Pratteln, Switzerland.
[3]Now at Norges Geologiske Undersøkelse, Trondheim, Norway.
[4]Geological Institute, ETH-Zurich, Zurich, Switzerland.
[5]Swiss Seismological Service, ETH-Zurich, Zurich, Switzerland.

0148-0227/07/2006JB004723$09.00

face. Yet, detailed knowledge on the kinematic and dynamic conditions of mountain slopes is essential for understanding and predicting catastrophic rockslide failures [*Kilburn and Petley*, 2003; *Eberhardt et al.*, 2004a; *Stead et al.*, 2006]. To tackle this issue, traditional methods for determining movements in unstable regions that require geodetic networks and point strain measurements [*Dunnicliff*, 1988; *Jaboyedoff et al.*, 2004] are being complemented by modern GPS, interferometric synthetic aperture radar, and airborne laser altimetry techniques [*Antonello et al.*, 2004; *Hilley et al.*, 2004; *Catani et al.*, 2005; *Metternicht et al.*, 2005; *Bulmer et al.*, 2006; *Burgmann et al.*, 2006; *Glenn et al.*, 2006], all of which are capable of supplying high-resolution displacement data over large areas.

[5] In addition to these purely kinematic techniques, studies of microseismic activity have the potential to provide information crucial for improving our understanding of mountain slope instabilities. Microseismic monitoring can be used to track the movements of various types of material. It is a well established method in studies of volcanoes [*Vilardo et al.*, 1996; *De Natale et al.*, 1998; *Lomax et al.*, 2001; *Pezzo et al.*, 2004; *Presti et al.*, 2004; *Lippitsch et al.*, 2005], fracturing and fluid flow in hydrocarbon reservoirs and hot dry rock systems [*Rutledge et al.*, 1998; *Vécsey et al.*, 1998; *Oye and Roth*, 2003; *Evans et al.*, 2005], mining-induced earthquakes [*Trifu and Urbancic*, 1996; *Iannacchione et al.*, 2005], and major tectonic faulting [*Malin et al.*, 1989; *Schorlemmer and Wiemer*, 2005]. It is starting to play an increasingly important role in investigations of unstable hill and mountain slopes [*Rouse et al.*, 1991; *Eberhardt et al.*, 2004b; *Amitrano et al.*, 2005; *Brückl and Parotidis*, 2005; *Merrien-Soukatchoff et al.*, 2005; *Roth et al.*, 2006].

[6] As part of a multidisciplinary effort to understand the physical processes that lead to mountain slope instability and failure [*Eberhardt et al.*, 2001, 2004a, 2004b; *Willenberg et al.*, 2002, 2003; *Willenberg*, 2004; *Heincke et al.*, 2005, 2006a, 2006b; *Green et al.*, 2006; *Spillmann et al.*, 2007], we have been monitoring microseismic activity across a well-studied mountain slope that lies directly above a scarp generated by the largest rockslide in recent Swiss history. Many of the following issues confronted during our pilot microseismic study are likely to influence microseismic investigations of other collapsing mountainous terrains: (1) dangerously steep slopes (Figures 1b and 1c) limited the emplacement of seismic sensors, such that the aperture of the microseismic network was less than optimal, (2) the inevitable harsh weather conditions and remoteness of the high mountain made it difficult to maintain continuous operation of the network during its 31-month lifetime, (3) the recorded data were plagued with noise transients, some of which were undoubtedly caused by atmospheric electrical discharges (e.g., near and distant lightening storms) and other electrical disturbances associated with the resistive environment of the high mountain and the long recording cables, (4) *P* wave seismic velocities of the crystalline rocks varied abruptly from very low values of <1.5 km/s to more normal values of >3.8 km/s, such that locating the microearthquakes in the extremely heterogeneous environment was a major challenge, and (5) strong scattering and absorption resulted in most seismograms having rather emergent *P* phases and generally complex codas with only poorly identifiable *S* phases.

[7] After briefly introducing the study site and results of related geological and geophysical investigations, we describe the essential details of our microseismic monitoring system. We then focus on the detection and location of microearthquakes within the unstable rock mass, emphasizing the importance of our independently determined 3-D tomographic velocity model and the probabilistic approach we employ for estimating the hypocenter parameters. We conclude with an integrated interpretation of the resultant microseismicity pattern, displacement rates defined by point strain estimates, and major fracture zones/faults.

2. Randa Study Site

2.1. The 1991 Randa Rockslides

[8] As a result of two major rockslides during the spring of 1991, approximately 30 million m^3 of crystalline rock plunged into the Matter Valley from a high mountain slope overlooking the village of Randa in southwest Switzerland (Figure 1) [*Schindler et al.*, 1993; *Sartori et al.*, 2003]. The dislodgement of the rock created a ~700 m high scarp on the side of the mountain and a huge debris cone that obliterated holiday apartments and barns, blocked the only land route to the major tourist resort of Zermatt, and dammed the Mattervispa River, causing flooding in upstream areas of the valley.

2.2. Geology and Fracture/Fault Systems

[9] Our knowledge of the geology of the mountain slope is based on extensive rock outcrops (Figures 1b and 1c), analyses of aerial photographs, and interpretations of optical televiewer and geophysical logs recorded in three moderately deep boreholes (SB120, SB50S, and SB50N with lengths of 120.8, 52.2, and 51.0 m, respectively; Figure 1c). The upper part of the slope is dominated by heterogeneous gneisses with a strong 20–25° west-southwest dipping foliation and three major fracture zone/fault systems [*Willenberg*, 2004]. One system parallels the bedrock foliation. Fracture zones/faults of this system can be traced on surface-based 3-D georadar data from their exposures at the surface to 10–20 m depth [*Heincke et al.*, 2005, 2006a]. The other two systems are steeply dipping, with strikes ranging from northeast-southwest to northwest-southeast (Figure 2a). Borehole georadar reflection data and semblance-migrated versions of the surface-based georadar data allow many steeply dipping fracture zones/faults to be mapped to depths as great as 75 m [*Heincke et al.*, 2006a; *Spillmann et al.*, 2007]. The instability of the mountain slope appears to be strongly influenced by the steeply dipping fracture zones/faults, some of which have openings of tens of centimeters and are actively moving [*Willenberg*, 2004; *Spillmann et al.*, 2007].

3. Randa Monitoring Systems

3.1. Geodetic-Geotechnical-Meteorological Monitoring Systems

[10] Shortly after the 1991 rockslides, a monitoring system comprising geodetic reflectors, surface extensome-

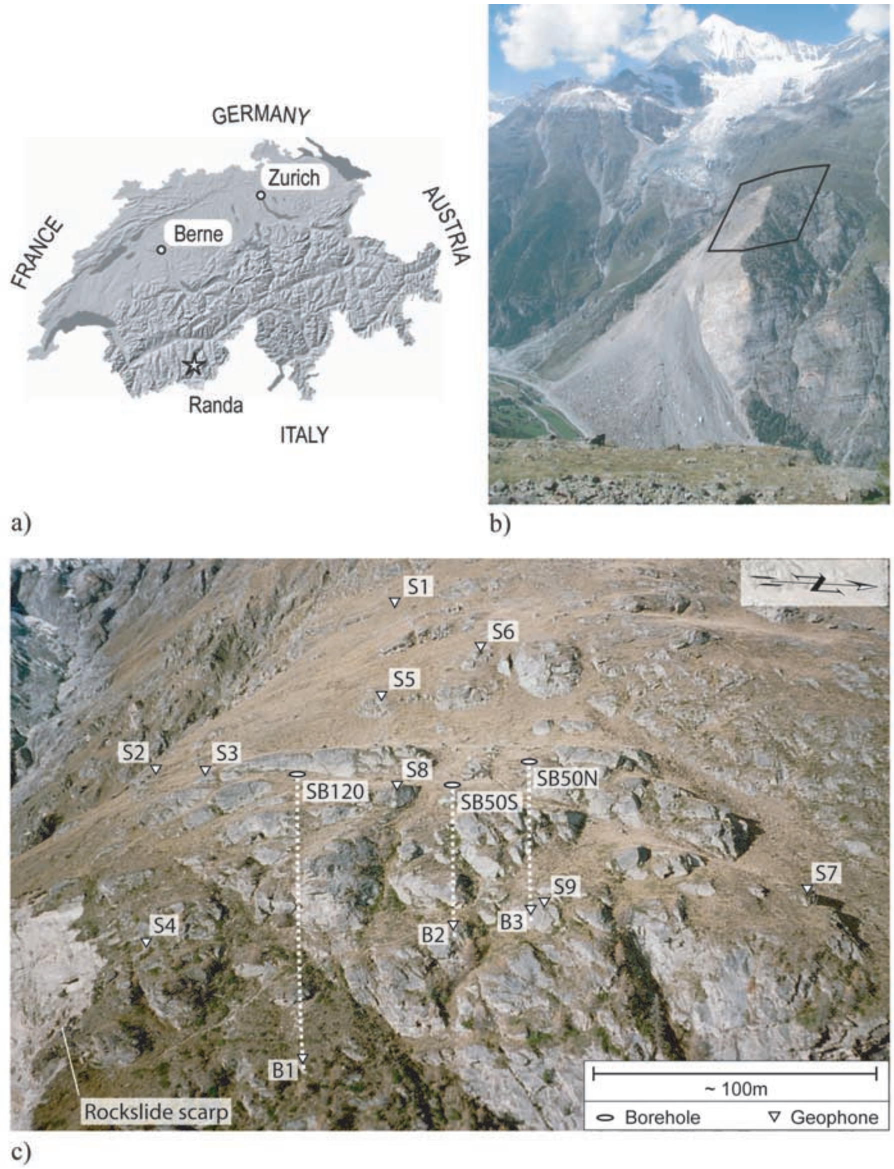

Figure 1. (a) Location (star) of the Randa study site in the Matter Valley of southern Switzerland. (b) Photograph of the Randa rockslide and study site. (c) Photograph highlighting the rugged nature of the terrain on which the microseismic network was deployed. SB120, SB50S, and SB50N are boreholes, with dotted lines showing schematically their lengths within the crystalline rock. S1–S9 are near-surface geophones. B1–B3 are borehole geophones. Photographs are by H. Willenberg and B. Rinderknecht.

ters, and meteorological stations was installed on the mountain slope [*Jaboyedoff et al.*, 2004]. The distances of the geodetic reflectors to various stable points have since been monitored using an electronic distance meter and the relative positions of selected reflectors have been determined via triangulation. At the beginning of our project, an independent geotechnical monitoring system was established. It included borehole extensometers, inclinometers, and piezometers and additional surface extensometers [*Willenberg*, 2004; *Spillmann et al.*, 2007]. Some of these new instruments supplied data on a semicontinuous basis (i.e., single observations every 6 min) to the ETH data processing laboratory via links to the microseismic system (Figure 3; see section 3.2), whereas others provided data only when accessed by on-site personnel.

[11] The geodetic observations and surface displacement measurements suggest that 2.7–9.2 million m^3 of the rock mass is moving southwestward toward the scarp at 1–2 cm/yr (see solid arrows in Figures 2a and 2b) [*Eberhardt et al.*, 2001; *Jaboyedoff et al.*, 2004; *Willenberg*, 2004]. Displacements at the surface are greatest near the scarp, decreasing to zero at distances >150 m from the scarp edge, whereas those in the boreholes appear to be concentrated at the intersections of major discontinuities. Most significantly, movements have been detected near the base of borehole SB120, suggesting that instabilities extend to >120 m depth (Figures 1c and 2b) [*Willenberg*, 2004].

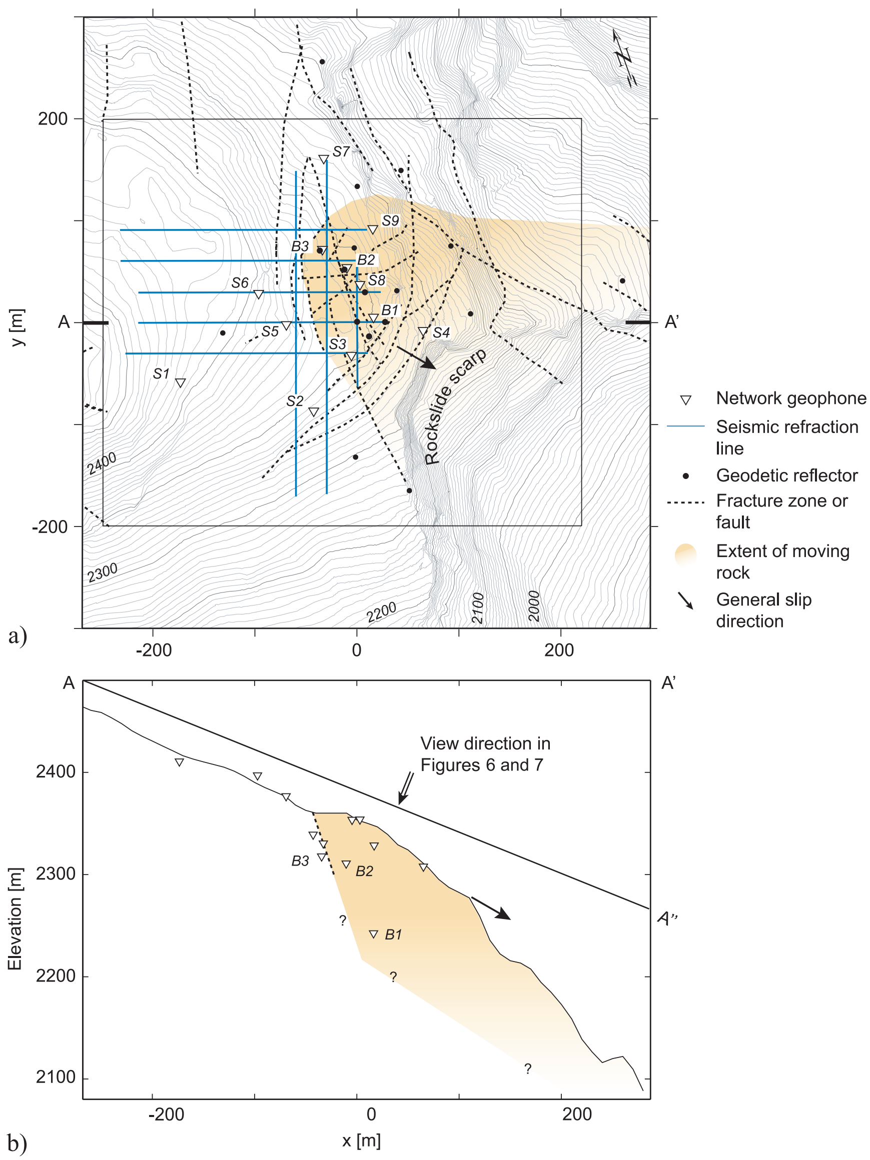

Figure 2. (a) Map outlining the locations of the network geophones (S1–S9; B1–B3), 3-D refraction seismic lines, geodetic reflectors, fracture zones and faults (mostly steep dipping), and estimated extent of mobile rock based on geodetic and geotechnical information. Geophones B1, B2, and B3 are near the bottoms of boreholes SB120, SB50S, and SB50N, respectively (see Figure 1c). The inner rectangle delineates the boundaries of maps presented in Figures 11, 13, 15, and 16. (b) Locations of the network geophones are projected on to cross section A–A′. Line A–A″ is a side view of the plane represented in Figures 6a, 7a, and 7c.

3.2. Microseismic Monitoring System

[12] Our microseismic network was deployed across topographically rugged terrain above the rockslide scarp at elevations of 2285–2450 m (Figures 1c and 2). It included nine three-component 8 Hz geophones (S1–S9) in 0.3–4.6 m deep holes and three three-component 28 Hz geophones (B1–B3) at depths of 113.5, 42.7, and 43.2 m in boreholes SB120, SB50S, and SB50N, respectively. Positions of the outermost network geophones S2, S4, and S7 were limited by the dangerously steep slopes at greater distances (Figure 1c). The maximum north-south and east-west apertures of the network (i.e., the distances between the furthest geophones) were both ~250 m.

[13] The microseismic data acquisition system and the ETH geotechnical equipment were designed to operate under harsh weather conditions in an isolated high-mountain environment. Analog cables connected the geophones to two Geode 24-bit multichannel seismographs and the geotechnical sensors to A/D converters and a data logger. Solar panels and a wind generator were the principal sources of energy for all instruments. When there was neither sun nor wind, large battery packs ensured autonomous operation of the instruments for approximately 10 days. The battery packs were recharged during subsequent sunny/windy periods.

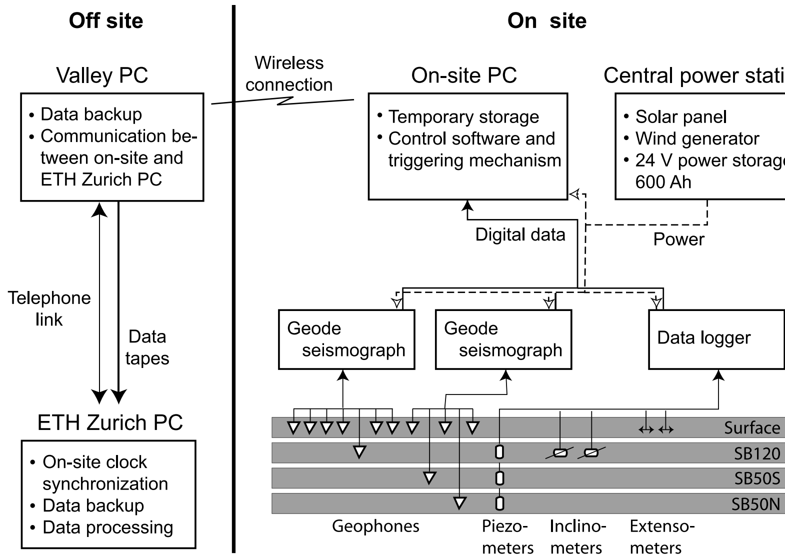

Figure 3. Sketch of the ETH microseismic and geotechnical monitoring systems.

[14] An on-site field PC controlled the entire data acquisition system and temporarily stored large volumes of triggered microseismic data. To detect microearthquakes, we employed a standard trigger algorithm based on short-time averages (STA) and long-time averages (LTA) of the incoming signals. For example, by setting the lengths of the STA and LTA windows to 40 and 500 ms, respectively, a single station was considered to have triggered when STA/LTA $\geq$ 40. A single trigger resulted in the recording of 8 s of data from all 12 three-component geophones. The data were sampled at a rate of 8000 Hz.

[15] All data were transferred to a desktop PC in the valley below to be temporarily stored and written to tapes that were regularly shipped to the ETH data processing laboratory. A land telephone link enabled us to access the desktop PC in the valley and through a radio connection between the desktop and on-site field PCs we were able to control the data acquisition system. During its 31-month deployment, the microseismic system was fully operational 81% of the time. For a 3-month period in 2002, the operational parameters of the system were reconfigured to allow the network to become an important component of the 3-D tomographic seismic refraction survey [*Heincke et al.*, 2006b].

4. Initial Processing of the Randa Microseismic Data

[16] A total of 66,409 triggered events were recorded between 1 January 2002 and 31 July 2004, corresponding to approximately 1 Terabyte of data. A selection of the various types of event is presented in Figure 4. To identify efficiently recordings generated by microearthquakes in the vicinity of the unstable mountain slope, we first designed and implemented a semiautomatic two-step pattern recognition procedure (Appendix A). Those events recognized by this procedure as possible microearthquakes were then analyzed manually. Application of this combined scheme led to the identification of (1) 55,563 noise transients generated by electrical disturbances, (2) 10,432 recordings that contained either noise, low-coherency events, generally weak signals, or emergent signals probably originating from distant earthquakes and explosions, (3) 206 regional earthquakes (such events often occur in the western Swiss Alps [*Maurer and Kradolfer*, 1996]), and (4) 223 mountain slope events comprising 129 sequences of multiple microearthquakes and 94 single microearthquakes. The microearthquake recordings were characterized by moderately high frequencies (mostly < 200 Hz) and short durations.

[17] Unfortunately, the overall data quality of the mountain slope microearthquake recordings was not high. Only about ten tremors generated seismograms with signal-to-noise ratios as high as the single event shown in Figure 4. Nevertheless, we could pick 2118 first-arrival *P* wave times for the 223 single and multiple microearthquakes (first-arrival times were only picked for the most prominent event in any sequence). The first-arrival times were defined by the earliest of the onsets detected by the three-component geophones. A minimum of five first-arrival *P* wave times was available for all 223 microearthquakes.

[18] Although polarization analyses demonstrated the presence of *S* wave energy in many seismograms, it was extremely difficult to determine *S* wave onset times with sufficient accuracy to be useful for microearthquake location purposes. Furthermore, coherent *S* wave arrivals were not observed on any microearthquake seismic section (i.e., plots of the recorded data arranged according to their first-arrival times). There were a variety of possible explanations for this: (1) Extensional faulting on the ubiquitous fractures likely generated earthquakes with strong nondouble-couple components and correspondingly weak *S* phases [*Julian et al.*, 1998; *Miller et al.*, 1998]. (2) As a consequence of the moderate frequency content of all microearthquake recordings, the first *P* wave pulse or its coda interfered with the first *S* wave arrivals at all geophones close to the events. (3) The very strong velocity contrasts of the mountain slope rocks (see section 5) undoubtedly resulted in the generation of *P*-to-*S* converted waves, which again would have interfered with the pure *S* waves; because of strong velocity heterogeneity, the effects would have been different at

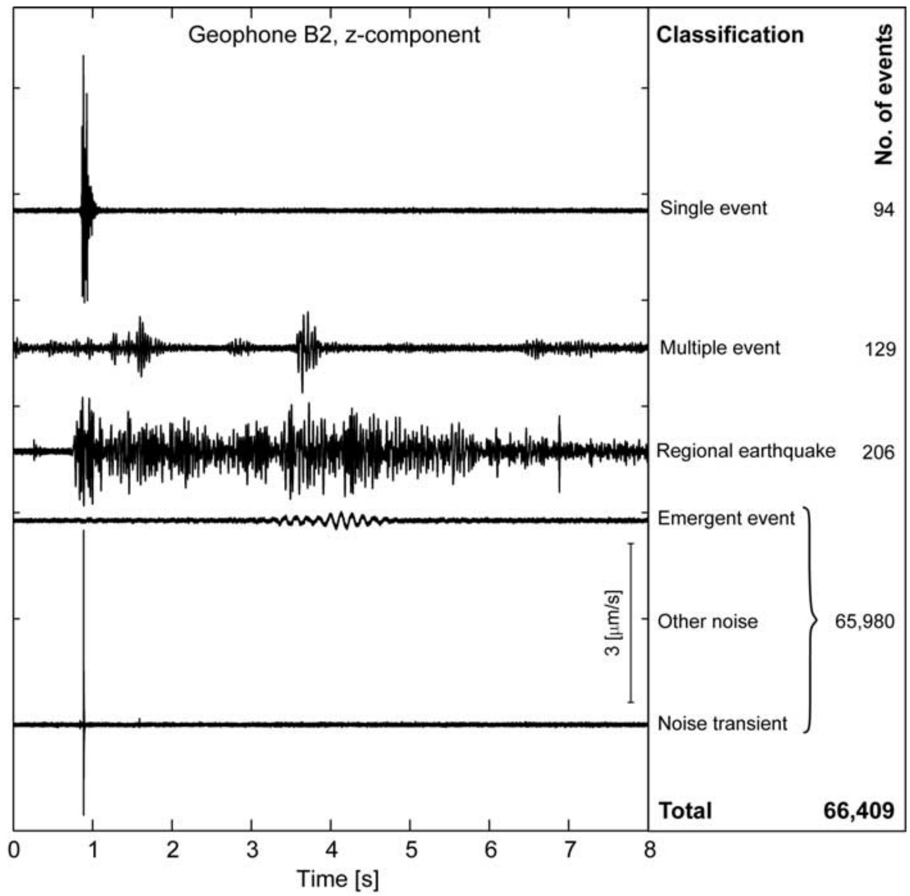

Figure 4. Examples of seismograms recorded at the Randa study site plotted using a common amplitude scale. Most single and sequences of multiple events are likely related to rockslide activity. The emergent events probably originate from distant earthquakes. Numerous regional earthquakes occur in the western Swiss Alps.

different azimuths relative to the microearthquakes. (4) Finally, the moderate frequency content of the recordings at short distances suggests that anelastic attenuation was generally high, such that *S* wave energy would have suffered significant absorption.

5. A 3-D Seismic Velocity Model

[19] An accurate velocity model is required for reliably locating earthquakes in highly heterogeneous media [*Lomax et al.*, 2000, 2001; *Husen et al.*, 2003; *Husen and Smith*, 2004; *Presti et al.*, 2004]. It is especially important for earthquakes located near or outside the boundaries of microseismic networks and/or for traveltime data sets lacking reliable *S* wave information. To obtain the necessary detailed velocity information, we benefited from a comprehensive 3-D tomographic seismic refraction survey across a large region of the mountain slope [*Heincke et al.*, 2006b].

[20] Our 3-D seismic refraction survey comprised five profiles parallel to the general downslope direction, three profiles perpendicular to it, 33 source locations slightly offset from the profiles, and the 12 three-component geophones of the microseismic network (Figure 2a). Source and geophone spacings along the 126–324 m long profiles were 4 and 2 m, respectively. Small explosive charges of 5–50 g detonated in 0.5–0.7 m deep holes provided the sources of seismic energy; only small charges were used to avoid damaging the sensitive high-alpine environment and possibly increasing mountain slope instability. Shots along the profiles were recorded by geophones along the respective profiles and by the entire microseismic network, whereas shots at the offset source locations were recorded on geophones along all profiles and, again, by the entire network.

[21] From the >99,000 recorded traces we were able to pick 52,600 first arrivals with an accuracy of better than ~5 ms. A 3-D tomographic inversion of these traveltimes revealed a highly heterogeneous rock mass dominated by a broad northeast-southwest trending zone of remarkably low seismic velocities (Figure 5a) [*Heincke et al.*, 2006b]. Velocities of <1.5 km/s occurred over a 200 × 100 m area extending to ~25 m depth and velocities of 1.5–2.7 km/s could be traced to various depths across a large segment of the mountain slope. Continuous tracts of rock with velocities >3.8 km/s were only found in the northwest part of the site. Blocks of relatively high-velocity material were detected within the mostly low-velocity regions and vice versa. *Heincke et al.* [2006b] suggested that the low velocities resulted from the presence of numerous dry cracks, fractures, and faults at a wide variety of length scales.

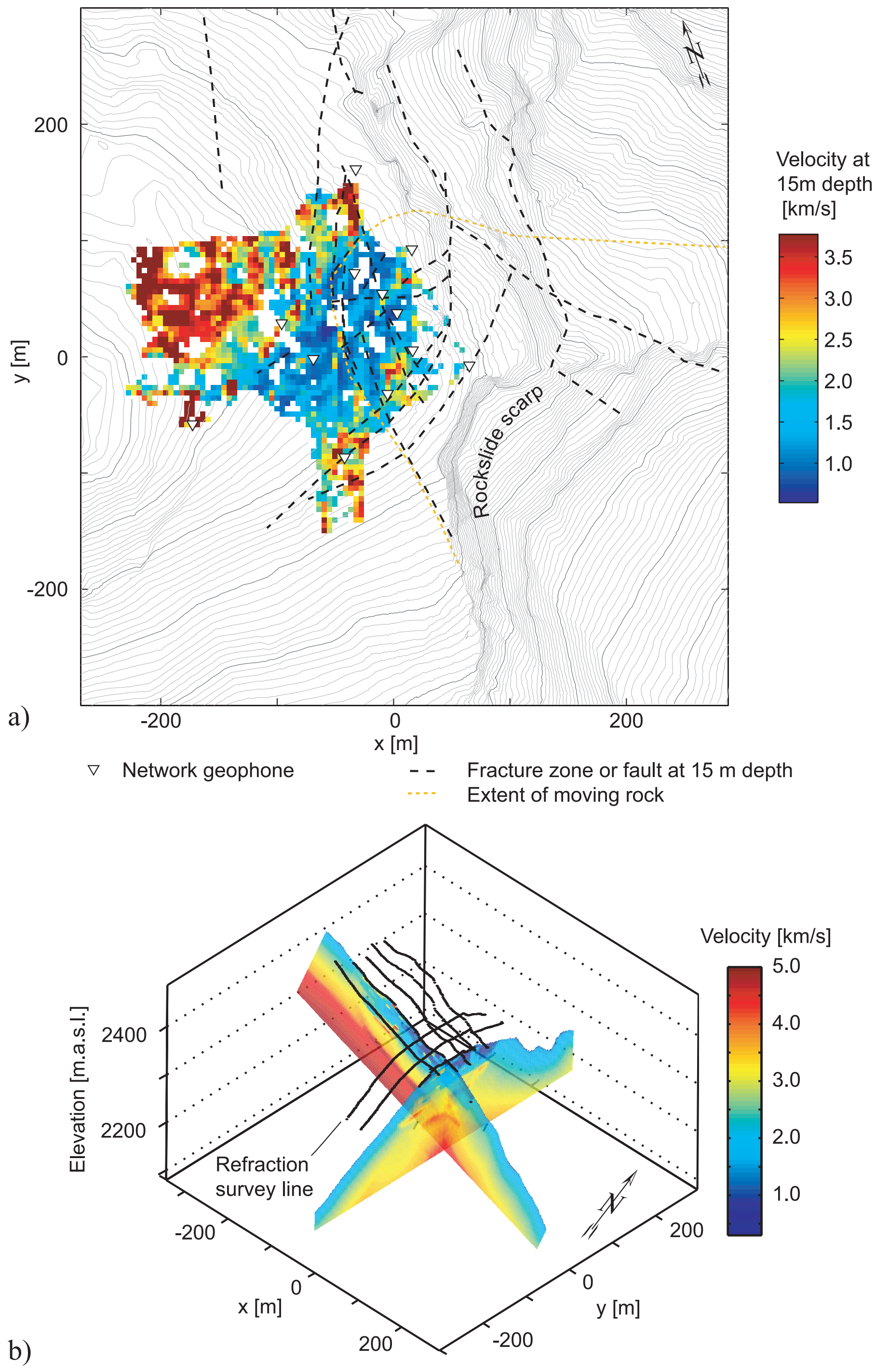

Figure 5. (a) P wave velocities extracted from *Heincke et al.*'s [2006b] tomographic model at 15 m depth below the surface (velocities >3.8 km/s are plotted with the same reddish brown color). Also displayed are fracture zones and faults projected to 15 m depth and the estimated extent of mobile rock based on geodetic and geotechnical information. Map boundaries are as for Figure 2a. (b) Two cross sections through the expanded 3-D velocity model shown in perspective view. Closely spaced dots (almost lines) identify geophones deployed for the tomographic survey.

[22] To account for the possibility that some microearthquakes occurred exterior to the microseismic network boundaries, it was necessary for us to define velocities beyond the limits of the 3-D velocity model. For this purpose, we derived from the 3-D velocity model an average 1-D velocity model that followed the topography and then expanded the volume of investigation to include a much larger portion of the mountain slope. The 1-D velocity model was then employed as the initial input model for a new 3-D tomographic inversion. Well-constrained velocities

within the new model, which matched those of the original 3-D model, graded relatively smoothly to values defined by the input 1-D velocity model (Figure 5b). We emphasize the limited accuracy of velocities not explicitly determined from the 3-D tomographic survey data.

6. Determining Earthquake Locations

[23] It is clear that we need an earthquake location scheme that accounts for strong 3-D velocity heterogeneity. This scheme should also provide realistic estimates of location uncertainty in the presence of a variety of factors that cause the computational process to be ill-conditioned. These factors include the relatively large reading inaccuracies ($\sim$5 ms) of many first-arrival *P* waves, a paucity of first-arrival *P* wave times for some events, the lack of reliable *S* wave information, and the occurrence of a large number of tremors just outside of the microseismic network boundaries.

[24] Traditional methods for locating earthquakes involve iteratively solving linearized approximations to the equations that connect hypocenter parameters and origin times to the observed traveltimes and velocity structure of the Earth [*Lee and Stewart*, 1981]. Estimates of hypocenter parameter uncertainty, usually assumed to be normally (Gaussian) distributed, are provided by error ellipsoids defined by the diagonal elements of the model covariance matrix [*Menke*, 1989]. Although traditional methods work well in many circumstances, recent work based on synthetic and field examples and 1- and 3-D velocity models highlight their shortcomings when the inversion process is ill-conditioned [*Lomax et al.*, 2000; *Husen et al.*, 2003; *Presti et al.*, 2004; *Lippitsch et al.*, 2005]. Under such circumstances, the estimated locations may be far from the true ones and the estimated uncertainties may be highly inaccurate; the error ellipsoids may not even encompass the true event positions. Most importantly, the locations of earthquakes that appear to be well determined may transpire to be very poorly constrained when more exact techniques are employed [e.g., see *Lippitsch et al.*, 2005].

[25] As expected, traditional earthquake location methods provided flawed information at the Randa study site. Accordingly, to estimate the distribution of hypocenter parameters we have used the comprehensive nested-grid search version of *Lomax et al.*'s [2000] implementation of *Tarantola and Valette*'s [1982] nonlinear probabilistic location technique. This technique has previously been used to locate earthquakes in topographically rugged and highly heterogeneous volcanic terrains [*Vilardo et al.*, 1996; *De Natale et al.*, 1998; *Lomax et al.*, 2001; *Presti et al.*, 2004; *Husen and Smith*, 2004; *Lippitsch et al.*, 2005].

[26] As for the traditional methods, the input data to the nonlinear probabilistic location technique include the arrival times and geometry of the microseismic network, and a reliable representation of the Earth's velocity structure is needed. In addition, the probabilistic technique requires the uncertainties in the arrival times and theoretical traveltimes to be defined by probability density functions (PDFs). By using Gaussian distribution functions to represent these input PDFs, the output hypocenter PDFs can be analytically derived [*Tarantola and Valette*, 1982].

[27] It is relatively straightforward to incorporate arbitrarily complicated velocity models in the probabilistic location technique [*Lomax et al.*, 2000; *Presti et al.*, 2004]. To minimize computational effort, the traveltimes of seismic waves from the network geophones to all grid points are calculated and stored in the form of look-up tables. Considering that these calculations are usually only required once for a microseismic network, very accurate forward routines can be employed. For example, a 3-D version of *Podvin and Lecomte*'s [1991] finite difference eikonal solver provides accurate direct, diffracted, and head wave traveltimes in *Lomax et al.*'s [2000] scheme. For the probabilistic location of earthquakes, it is only necessary to access the look-up traveltime tables on a frequent basis.

[28] A hypocenter PDF provided by the nonlinear probabilistic location technique encompasses all likely solutions (i.e., it is a complete probabilistic solution) and includes comprehensive information on the effects of (1) uncertainties in the arrival times and theoretical traveltimes, (2) any incompatibility of arrival time picks, and (3) the spatial relationships between the network geophones and the earthquake locations. Although uncertainties in the arrival times and theoretical traveltimes are usually defined as Gaussian, the nonlinear relationships involved in the location process result in the solution uncertainties being non-Gaussian (i.e., the error surface is no longer ellipsoidal). Indeed, the hypocenter PDFs may be highly irregular [*Lomax et al.*, 2000, 2001; *Husen et al.*, 2003; *Husen and Smith*, 2004; *Lippitsch et al.*, 2005; *Lomax*, 2005].

[29] In most earthquake studies, uncertainty can be readily estimated for each arrival time pick, but uncertainties in the theoretical traveltimes (i.e., inaccuracies in the velocity model) are generally poorly known. This is an important limitation in many investigations, because errors in the velocity model may result in systematically biased locations, especially near and outside the boundaries of microseismic networks [*Lomax et al.*, 2000].

[30] For the location of all events in our study, uncertainties are defined by a Gaussian distribution function that represents the $\sim$5 ms reading accuracy of many first arrivals and a Gaussian distribution function that represents a 0.2 ms inaccuracy in the theoretical traveltimes. Although our extended 3-D model is generally well constrained throughout much of the investigation volume, it certainly does not include all small-scale velocity heterogeneities that influence the *P* wave arrival times. To compensate partly for this shortcoming, we compute and apply station corrections that minimize errors in locating a number of calibration shots (see section 7.2). Furthermore, we demonstrate the sensitivity of our microearthquake locations to variations in the theoretical traveltimes by comparing hypocenters obtained using our 3-D model with those obtained using a constant velocity model.

[31] We display a hypocenter in three forms: (1) a PDF scatter cloud in which the densities of dots are proportional to the probabilities (each hypocenter PDF is represented by 1000 dots and the volume integral of all probabilities of a PDF is normalized to a value of 1) or (2) PDF volumes shown in planar sections by a color-scale representation, and (3) a maximum-likelihood location. Scrutiny of the PDF scatter cloud or volume allows us to estimate the level and type of uncertainty. As examples, tightly grouped dots

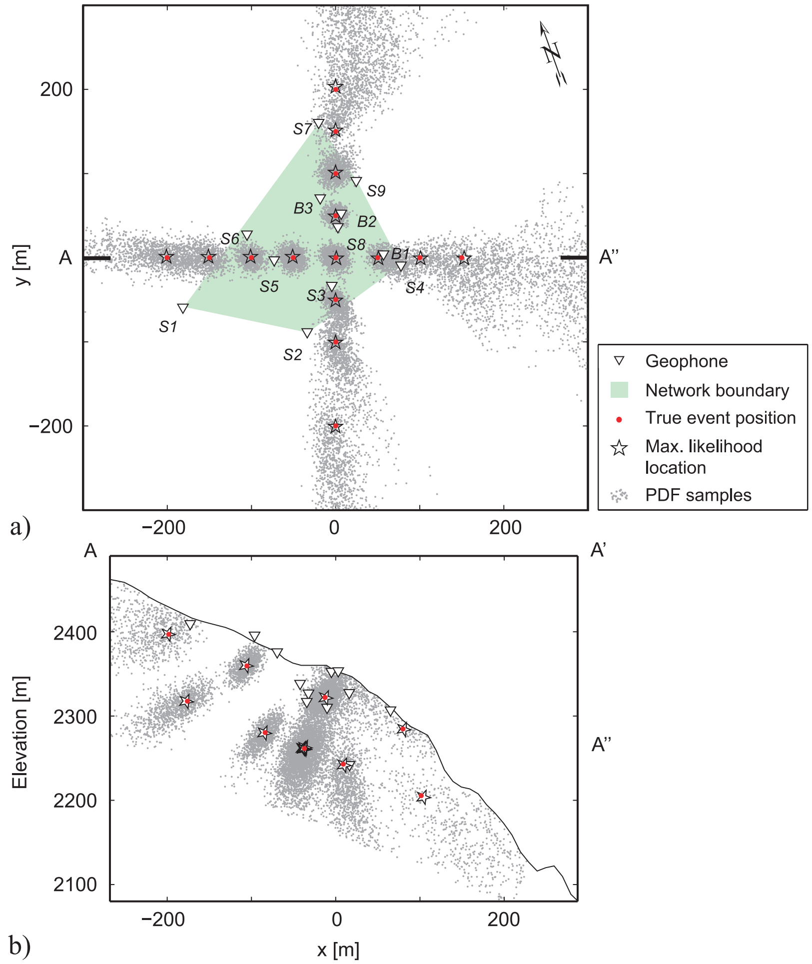

Figure 6. Estimating the resolution of the microseismic network for a sequence of events along two planes within a homogeneous velocity model (velocity of 2.5 km/s). Both diagrams show projections of all network geophones, true event locations, complete PDF scatter clouds, and maximum-likelihood locations. (a) Map boundaries are the same as for Figure 2a, but the viewing direction is approximately perpendicular to the dipping surface (see Figure 2b). Note the near-perfect correspondence between the true and maximum-likelihood event locations. (b) Various details projected on to cross section A–A″.

in the PDF scatter cloud (i.e., a small PDF volume) are evidence for a well-resolved hypocenter, whereas broadly scattered dots in all directions (i.e., a large PDF volume) indicate a poorly constrained one. A tight grouping of dots in the x-y plane and a broad scatter in the z direction (i.e., a narrow elongated PDF volume) are diagnostic of an event that has a well-resolved epicenter but a poorly constrained depth. Although there may be multiple acceptable solutions, we choose the maximum-likelihood (or minimum misfit) point of the hypocenter PDF as the optimum location.

7. Performance of the Randa Microseismic Network

7.1. Effect of Network Size and Geometry on the Hypocenter Estimation Process

[32] The size and geometry of the Randa microseismic network was controlled by (1) the position of the steep rockslide scarp and generally rugged topography (Figures 1 and 2), (2) our preference to have the geophones located on or within the bedrock, (3) a limit on the number of three-component geophones available for the 31-month duration of the project, and (4) the need for the geophones to be reasonably close to the two Geode seismographs and power sources (Figure 3) to minimize cable lengths and thus the effects of atmospheric and ground-based electrical disturbances. To determine the influence of the network's size and geometry on the hypocenter estimation process, we performed a simple synthetic experiment in which the effects of velocity heterogeneity and uncertainties in arrival time picks were explicitly excluded. We created a model that simulated the 3-D topography of the unstable mountain slope, the true locations of the microseismic network of geophones, and 16 earthquakes situated at different depths within two planes (Figure 6). Constant *P* wave velocities above and below ground level were set to 0.3 and 2.5 km/s, respectively. Noise-free arrival times were determined for *P* waves traveling from the simulated earthquakes to all network geophones. We then used the non-linear probabilistic location technique to determine the hypocenter PDFs and maximum-likelihood locations displayed in Figure 6. For this case and the calibration exercise described in section 7.2,

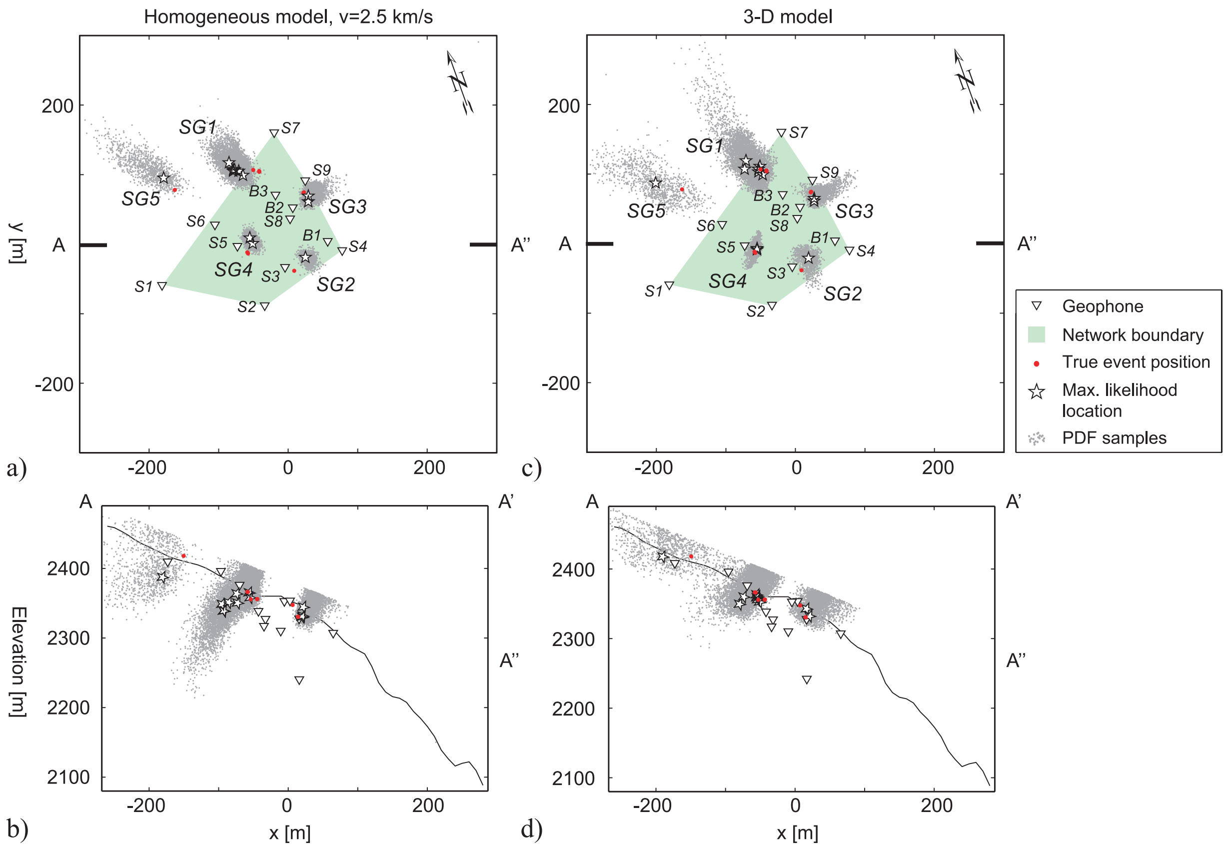

Figure 7. Calibration of the microseismic network using five groups of shots SG1–SG5. All diagrams show projections of all network geophones, complete PDF scatter clouds, and maximum-likelihood locations. (a) and (b) Results based on a homogeneous model with velocity of 2.5 km/s. (c) and (d) Results based on our extended 3-D velocity model. Map boundaries of Figures 7a and 7c are the same as for Figure 2a, but the viewing directions are approximately perpendicular to the dipping surface (see Figure 2b). In Figures 7b and 7d, various details are projected on to cross section A–A″. Several of the shots are very close together, such that only 6 of the 12 can be distinguished.

we allowed the grid search program to seek solutions above the ground to the limit of the model space. In contrast, to locate the microearthquakes we excluded the region exterior to the rock mass from the search process.

[33] Although the maximum-likelihood locations coincide with the true hypocenters throughout the mountain slope (Figure 6), the varying shapes and sizes of the hypocenter PDF scatter clouds highlight the very different confidence levels assigned to each location estimate. Within the network boundaries, the scatter clouds are generally symmetric with diameters mostly less than 30 m in planes parallel to the mountain slope (Figure 6a) and somewhat elongated in planes perpendicular to it (Figure 6b). Elongation increases with hypocenter depth. Nevertheless, because geophones are located in moderately deep boreholes and distributed over a wide range of elevations, the well-known ambiguity in earthquake depth estimate is relatively minor in the top ~50 m of our study site. Outside of the network boundaries, the dimensions of the scatter clouds and resultant uncertainties in earthquake locations increase significantly. Since we allowed the search space to extend above the ground, earthquakes close to the surface and mountain edge are better determined than indicated by the sparse nature of their scatter clouds.

7.2. Calibration of the Network Using Small Test Shots: Station Corrections

[34] To enhance the accuracy of our hypocenter parameter estimates, we have calibrated the microseismic network using a number of small test shots detonated at various locations across the study site. These shots were not included in the derivation of the 3-D velocity model. Traveltimes from 12 of the test shots grouped together in five small areas (SG1–SG5 in Figures 7–9) were sufficiently well determined (~5 ms reading accuracy) to be useful in the calibration procedure. Two of the shot groups were positioned within the network (SG2 and SG4 in Figure 7), two were located along network boundaries (SG1 and SG3), and one was situated northwest of the network (SG5).

[35] We began by computing for each calibration shot the root-mean-square (RMS) difference between the observed traveltimes and predicted traveltimes based on the true shot location and six different velocity models: the extended 3-D velocity model of Figure 5b and five homogeneous models with velocities between 2.0 and 5.0 km/s. The RMS differences varied from 6 to 40 ms, with nine of the 12 differences below 10 ms based on the 3-D velocity model and three based on the 2.5 km/s constant velocity model (Figure 8a). To improve the traveltime predictions, we

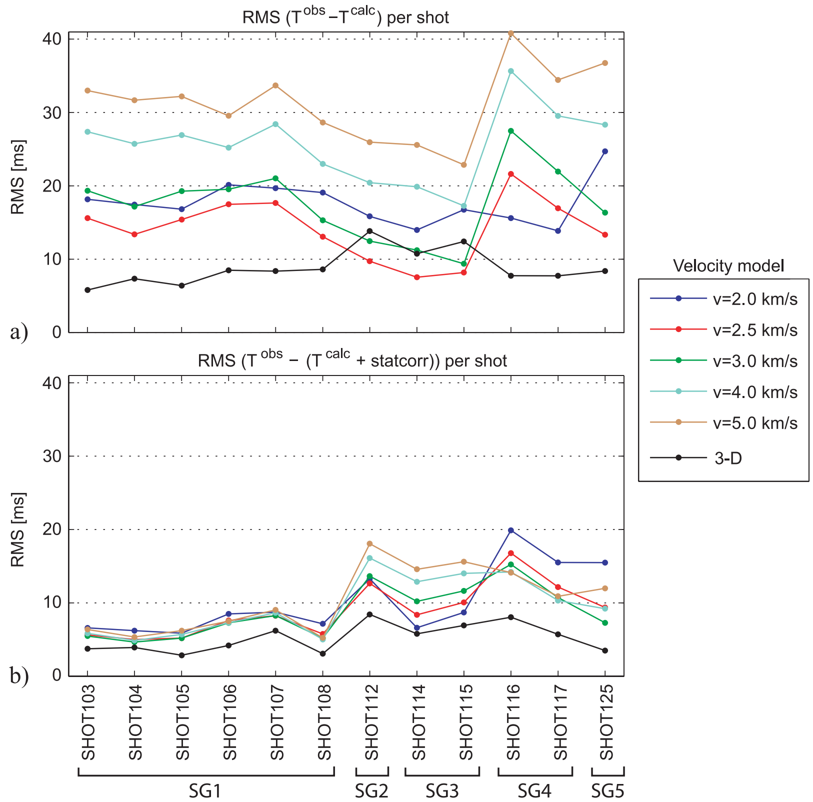

Figure 8. (a) Root-mean-square (RMS) differences between the observed traveltimes (T^{obs}) of the calibration test shots and computed traveltimes (T^{calc}) based on our extended 3-D model and a variety of homogeneous models. True shot positions were used for these computations. (b) Same as for Figure 8a, but after application of station corrections (statcorr). Shots are collected into five groups SG1–SG5 (see Figure 7).

averaged the traveltime differences at each geophone to produce a suite of azimuthally invariant station corrections for each velocity model; note that the geographic distribution of successful calibration shots was insufficient for the computation of azimuthally dependent station corrections. These corrections partly accounted for velocity model inadequacies close to the geophones. Application of the station corrections yielded substantially reduced RMS differences of

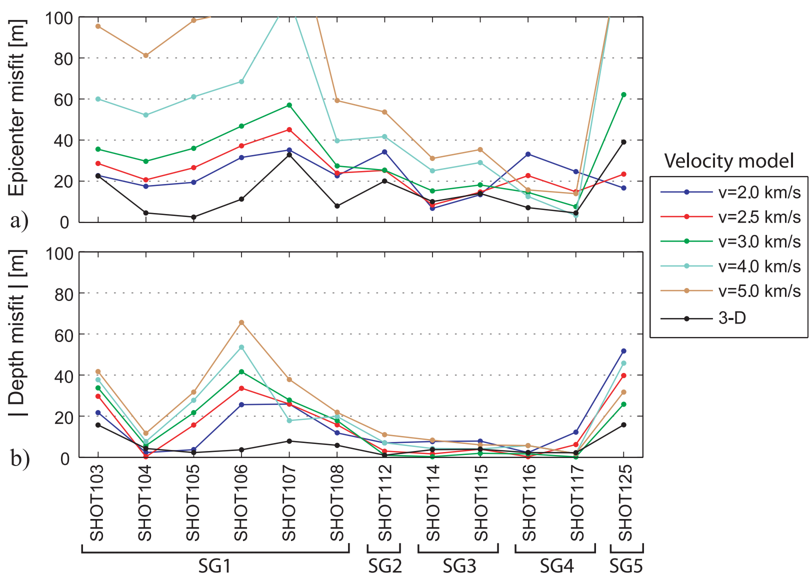

Figure 9. Accuracies of test shot maximum-likelihood locations based on our extended 3-D model and a variety of homogeneous models. (a) Absolute values of misfits between true and estimated epicenter locations. (b) Absolute values of misfits between true and estimated depths.

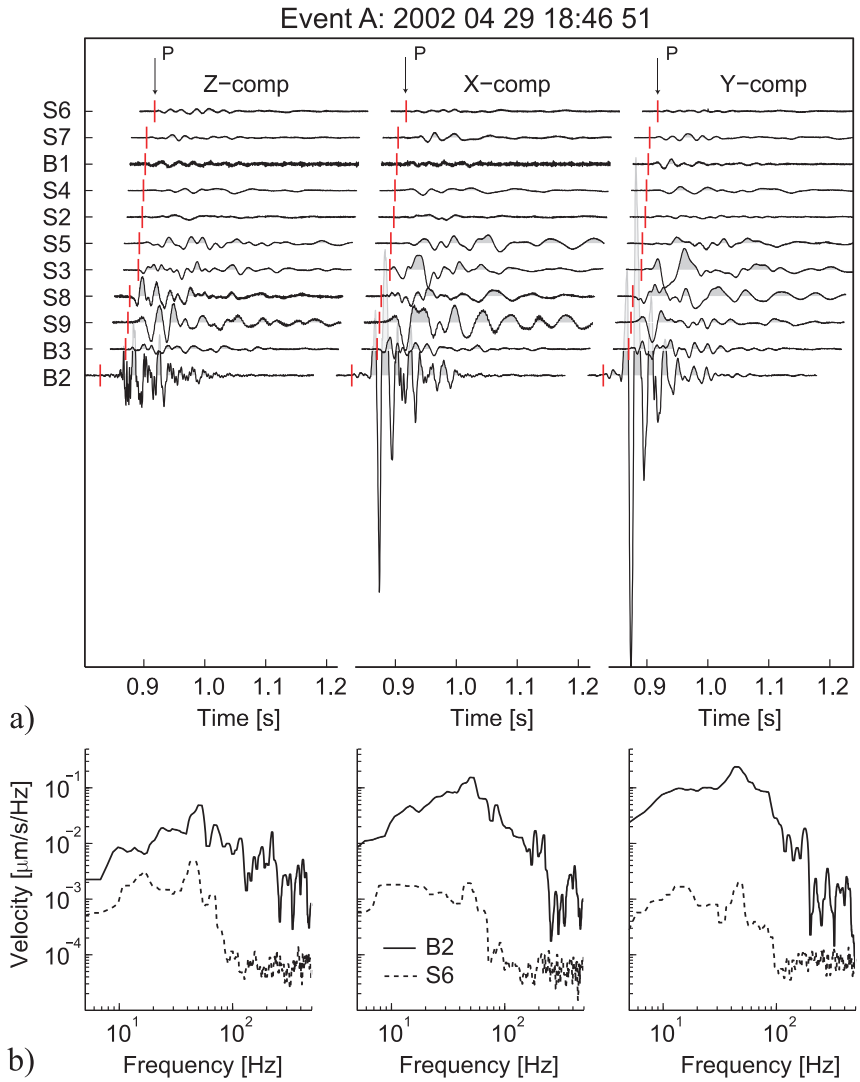

Figure 10. (a) and (c) Suites of three-component seismograms for two microearthquakes. (b) and (d) Spectra for selected seismograms. To enable direct comparisons to be made, a matching filter has been used to transform the 28-Hz geophone recordings of stations B1–B3 to effective 8-Hz geophone recordings. Traces are sorted according to first-arrival times. Event date and time are indicated above each suite of seismograms. The "P" ticks delineate picks of first arriving *P* waves, whereas the "S?" ticks show the approximate arrivals of *S* wave energy.

3–20 ms (Figure 8b), with the lowest values (3–8 ms) for all calibration shots based on the 3-D velocity model (Figure 8b). The average of the RMS differences for the extended 3-D velocity model calculations was ~5 ms, practically the same as the reading accuracy of many calibration shot and microearthquake recordings. We have applied station corrections to all recorded data sets before subjecting them to the nonlinear probabilistic location technique.

[36] Using the six velocity models, we determined the hypocenter PDFs and maximum-likelihood locations of the 12 calibration shots. As demonstrated by Figure 9, the absolute misfits of the maximum-likelihood locations were highly variable. The lowest misfits were mostly based on the 3-D velocity model, with the epicenters mislocated by 1–40 m (most mislocations were ≤21 m), and the depth estimates incorrect by 0–18 m (most depth errors were ≤8 m). The 2.0–3.0 km/s constant velocity models produced plausible hypocenter PDFs and maximum-likelihood locations for some calibration shots, but not for others. For example, Figures 7a and 7b show that several of the calibration shots occurred along the boundaries or completely outside of the PDF scatter clouds based on the constant 2.5 km/s model. By comparison, all calibration shots are enclosed by the respective hypocenter PDF scatter clouds based on the 3-D velocity model (the single shot of the SG2 group occurred along the boundary of its PDF scatter cloud; Figures 7c and 7d). As for the synthetic examples of Figure 6, the PDF scatter clouds in Figure 7 are markedly more compact for events inside the microseismic network than for those outside.

8. Microearthquake Locations and Magnitudes

[37] Despite the clear superiority of the extended 3-D velocity model, for comparison purposes we have estimated the hypocenter PDFs and maximum-likelihood locations of

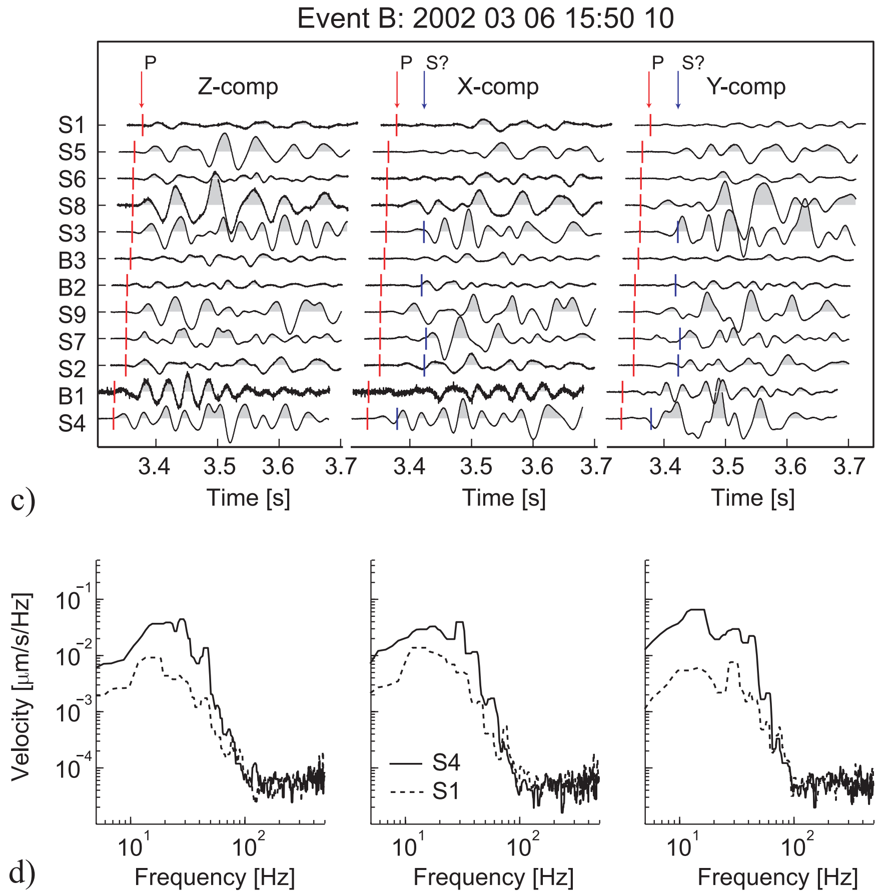

Figure 10. (continued)

all microearthquakes using both the 3-D and constant 2.5 km/s velocity models. We begin by describing probabilistic hypocenter parameters for two very different sets of recordings, one for a microearthquake clearly within the network (Figure 10a) and one for a microearthquke that was likely outside (Figure 10c), and then present the location results for the entire microearthquake data set.

8.1. Two Single Microearthquakes

[38] The hypocenter PDFs and maximum-likelihood locations for microearthquake A recordings (Figure 10a) are practically identical for computations based on the two velocity models (compare Figures 11a and 11c with Figures 11e and 11g). This event occurred directly above borehole geophone B2 (triangles showing the geophone position in Figures 11a and 11e are covered by the stars depicting the maximum-likelihood locations). The high-amplitude signals rich in high frequencies received by the three-component geophone B2 (frequency range 5–200 Hz) and the much lower amplitude signals largely devoid of high-frequency energy received by all other three-component geophones (frequency range 5–100 Hz; Figure 10a) are in accord with the derived maximum-likelihood locations and associated small PDF volumes.

[39] In contrast to microearthquake A, the hypocenter PDFs and maximum-likelihood locations for microearthquake B recordings (Figure 10c) are very different for the two velocity models (compare Figures 11b and 11d with Figures 11f and 11h). Yet the RMS differences between the observed and predicted arrival times are very similar for the two maximum-likelihood locations (i.e., 9.3 and 10.3 ms). Which of these two very different solutions should we accept: one with a relatively small PDF volume (i.e., seemingly well resolved) and a maximum-likelihood location that positions the event within the network very close to geophone S4 (Figures 11b and 11d) or one with a large PDF volume (i.e., poorly constrained) and a maximum-likelihood location that places the event southeast of the network near the rockslide scarp (Figures 11f and 11h)?

[40] There are two lines of evidence that support the second solution of a poorly constrained location exterior to the network. First, the recordings at geophone S4 do not contain the high frequencies expected of a nearby microearthquake (Figures 10c and 10d). Indeed, recordings at all geophones have similar low-frequency coda with comparably flat spectra in the narrow 5–50 Hz frequency band; amplitudes are more than 2 orders of magnitude lower for frequencies > 100 Hz than for frequencies < 50 Hz. Second, *S* wave energy appears to arrive 0.04–0.08 s after the first breaks detected on five of the three-component recordings displayed in Figure 10c. This assertion is supported by the results of the polarization analyses presented in Figure 12, in which the dominant particle motion directions are plotted as a function of arrival time for the five identified recordings;

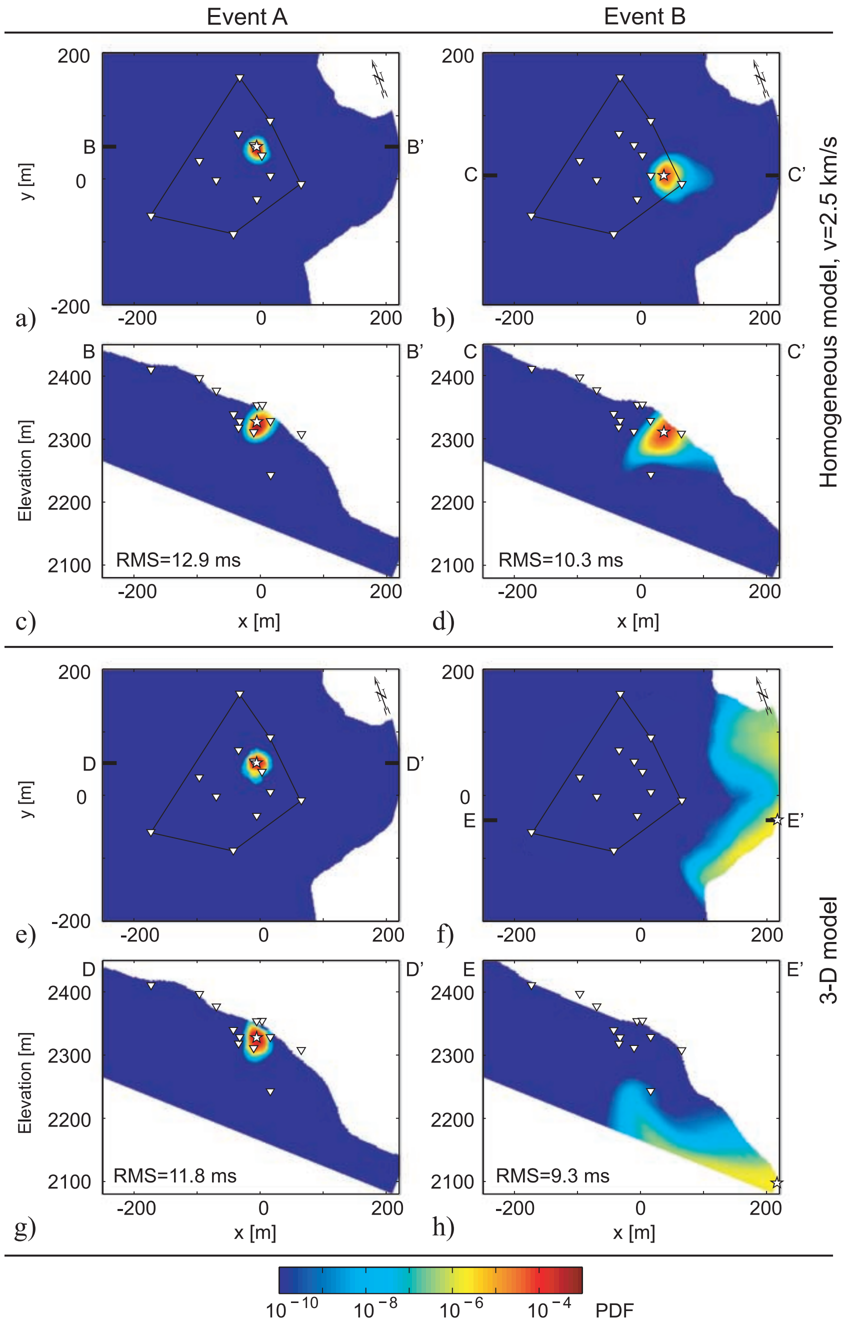

Figure 11. PDF volumes and maximum-likelihood locations (stars) of microearthquakes represented by the seismograms of Figure 10. Triangles, geophones. Lines connecting geophones delineate the outer limits of the microseismic network. (a)–(d) Results based on a homogeneous model with velocity of 2.5 km/s. (e)–(h) Results based on our extended 3-D velocity model. Figures 11a, 11b, 11e, and 11f are undulating sections through the PDF volumes at constant depths below the surface. The depths are defined by the respective maximum-likelihood locations of the microearthquakes. Map boundaries are as for the inner rectangle of Figure 2a. Figures 11c, 11d, 11g, and 11h are cross sections through the PDF volumes and maximum-likelihood locations with projected locations of geophones. RMS differences between the observed and predicted arrival times based on the maximum-likelihood locations are similar for the two velocity models.

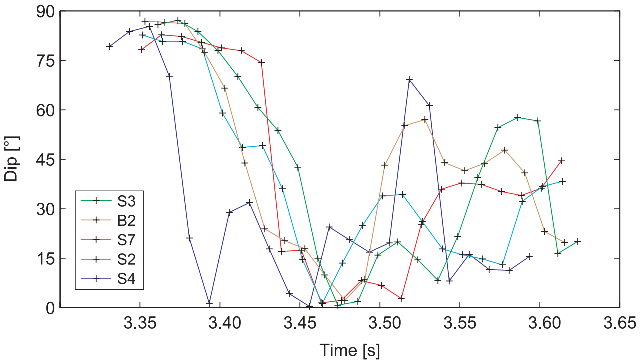

Figure 12. Results of selected polarization analyses of event B seismograms of Figure 10c showing the dominant angle of particle motion relative to the horizontal. For vertical incident rays, pure P and S waves have 90° and 0° dips, respectively.

the dominant particle motion directions were computed from the three-component recordings using the covariance technique introduced by *Flinn* [1965]. For a relatively distant event more than 100 m below the network (e.g., as shown in Figures 11f and 11h), the rays and P wave particle motions should be steeply dipping at the geophones and the S wave particle motions shallowly dipping. The opposite would be true for an event at the same depth level and close to the network (e.g., if the location shown in Figures 11b and 11d were to be correct). Particle motion directions are >70° for at least the first 0.04 s of the identified recordings (Figure 12). They change to shallowly dipping at later times, compatible with the arrival of S wave energy (near the second row of ticks in Figure 10c). Between 3.45 and 3.50 s, the particle motions of these recordings are practically horizontal. (Figure 12). The observed particle motion directions and the poorly resolved >0.04 s time gaps between the first P and S wave arrivals are consistent with the solution shown in Figures 11f and 11h, but not with that shown in Figures 11b and 11d.

8.2. Analysis of All Microearthquakes

[41] The maximum likelihood epicenters of all microearthquakes obtained for the two velocity models are displayed in Figures 13a and 13b. There are similarities and notable inconsistencies between the two epicenter patterns. Both show roughly half the events within the microseismic network and half outside and both include concentrations of shallow (i.e.,<30 m deep) events near to and beneath the rockslide scarp; a cluster of ~70 microearthquakes can be followed below a broad zone of the exposed scarp to well inside the network. Microearthquake A (Figures 10 and 11) is one of only a small number of well-resolved events that have practically identical maximum-likelihood locations based on the two velocity models. The well-resolved events are mostly situated within the network very close to one or more geophones. Maximum-likelihood locations of other events differ for the two suites of solutions. One consequence of these differences is the much tighter grouping of epicenters in Figure 13a than in Figure 13b. On the basis of our analyses of the calibration test shot and microearthquake B recordings, we conclude that the tightly clustered appearance of epicenters in Figure 13a is an artifact.

[42] Comparisons of the epicenter patterns in Figures 13a and 13b highlight uncertainties associated with inadequacies of the velocity models, but they take no account of the considerable uncertainties caused by arrival time inaccuracies and the less than optimal spatial relationships between the network geophones and many microearthquakes. Furthermore, the characteristics of each individual microearthquake are much less important in seismicity pattern analyses than the accumulative characteristics of many such events. For example, a single low-magnitude tremor is unlikely to influence greatly the stability of the mountain slope, but many tremors along a limited number of structures could eventually be linked to catastrophic collapse. To address these points, we analyze the sum of hypocenter PDFs computed for all microearthquakes rather than the individual PDFs. Figures 13c–13f display slices and cross sections through the two resultant cumulative hypocenter PDFs (one for each velocity model). Within some favorable parts of the network, a cumulative hypocenter PDF may delineate active faults, whereas in others it may only provide sufficient information to distinguish between zones of seismic activity and inactivity [*Presti et al.*, 2004].

[43] As for the epicenter patterns of Figures 13a and 13b, the cumulative hypocenter PDFs in Figures 13c–13f reveal general correlations and significant discrepancies between the results provided by the two velocity models. High PDF values in the vicinity of the rockslide scarp and beneath the eastern half of the network are common to the two solutions, but the detailed PDF patterns differ markedly. In addition, the seemingly prominent microseismogenic zone that extends through the cross section of Figure 13e is not observed in Figure 13f.

[44] The contrasting hypocenter PDF patterns displayed for the two velocity models in Figures 7, 11, and 13 have demonstrated the importance of incorporating reliable velocity information in the microearthquake location process. For the computation of microearthquake magnitudes and interpretation of microseismicity at the Randa study site, we employ the cumulative hypocenter PDF and maximum-likelihood locations based on our extended 3-D velocity model.

8.3. Magnitudes

[45] We computed moment magnitude estimates m for microearthquakes recorded by the Randa microseismic network using the following formulas introduced by *Hanks and Kanamori* [1979]:

$$m = \frac{2}{3}\log M_0 - 6.1, \tag{1}$$

where

$$M_0 = \frac{4\pi\rho\nu_p^3 R\Omega_0}{U}, \tag{2}$$

M_o is the seismic moment, density ρ = 2.7 g/m^3, P wave velocity ν_P = 2.500 km/s, R is the hypocentral distance, Ω_0 is the long-period amplitude determined from the displace-

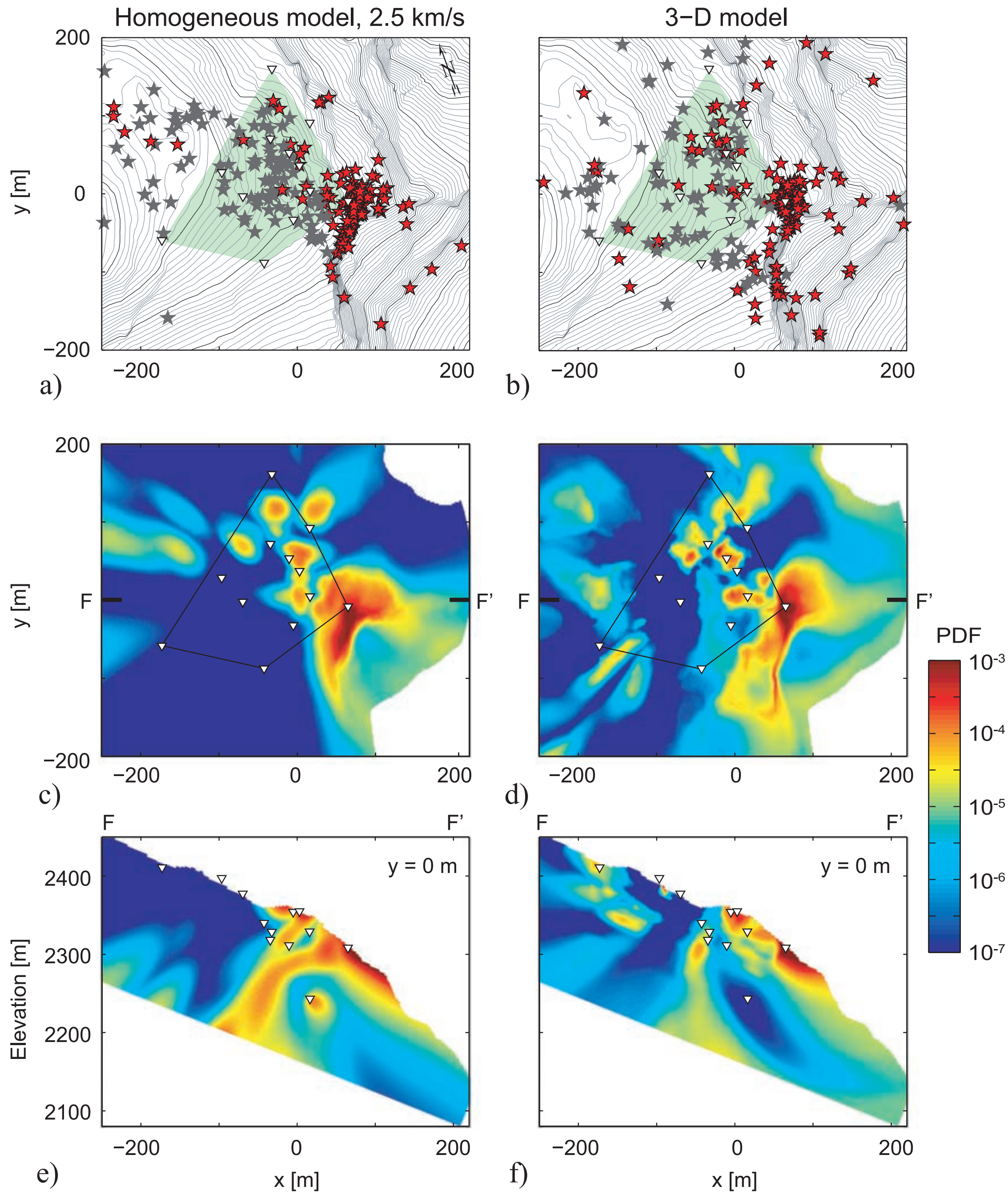

Figure 13. (a) and (b) Maximum-likelihood epicenters of all located microearthquakes. Triangles, geophones; red stars, shallow microearthquakes (depths $\leq$ 30 m below surface); gray stars, relatively deep microearthquakes (depths >30 m below surface). Light green shading delineates the extent of the microseismic network. (c) and (d) Undulating sections through the cumulative hypocenter PDF volumes at a constant 15 m depth below the surface. Lines connecting the geophones delineate the outer limits of the microseismic network. Map boundaries are as for the inner rectangle of Figure 2a. (e) and (f) Cross sections F–F′ with projected locations of geophones. Figures 13a, 13c, and 13e show results for a homogeneous model with velocity of 2.5 km/s. Figures 13b, 13d, and 13e show results for our extended 3-D velocity model.

ment spectra of isolated P waves, and U = 0.52 is a correction for the mean radiation pattern of P waves [*Aki and Richards*, 1980].

[46] Application of equations (1) and (2) using hypocentral distances based on the maximum-likelihood locations yielded estimates of m for all microearthquake recordings. Average moment magnitudes and standard deviations were then determined from the 5–12 estimates of m for each event. The resultant average moment magnitudes were

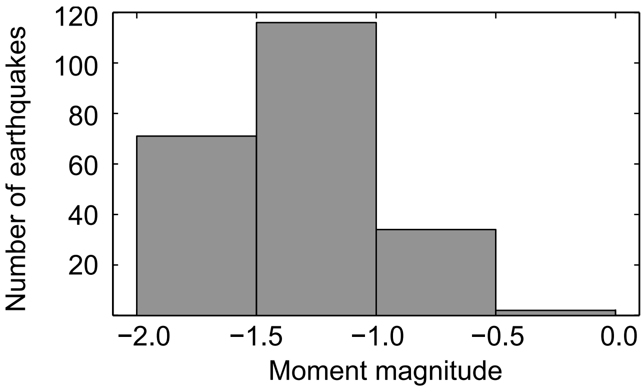

Figure 14. Histogram plot of Randa microearthquake moment magnitude estimates.

mostly in the -2.0 to -0.5 range with an average standard deviation of ± 0.2 (Figure 14).

9. Interpretation

[47] Our interpretation of microseismicity at the Randa study site is based on detailed analyses of the cumulative hypocenter PDF from different viewing angles (e.g., Figure 15) and comparisons of the PDF pattern with diverse geological, geodetic, geotechnical and other geophysical data (Figure 16) [*Eberhardt et al.*, 2001, 2004a, 2004b; *Willenberg et al.*, 2002, 2003; *Willenberg*, 2004; *Heincke et al.*, 2005, 2006a, 2006b; *Green et al.*, 2006; *Spillmann et al.*, 2007]. Various perspective views of the cumulative hypocenter PDF and slices and cross sections through it prove to be particularly useful. In the map and two perspec-

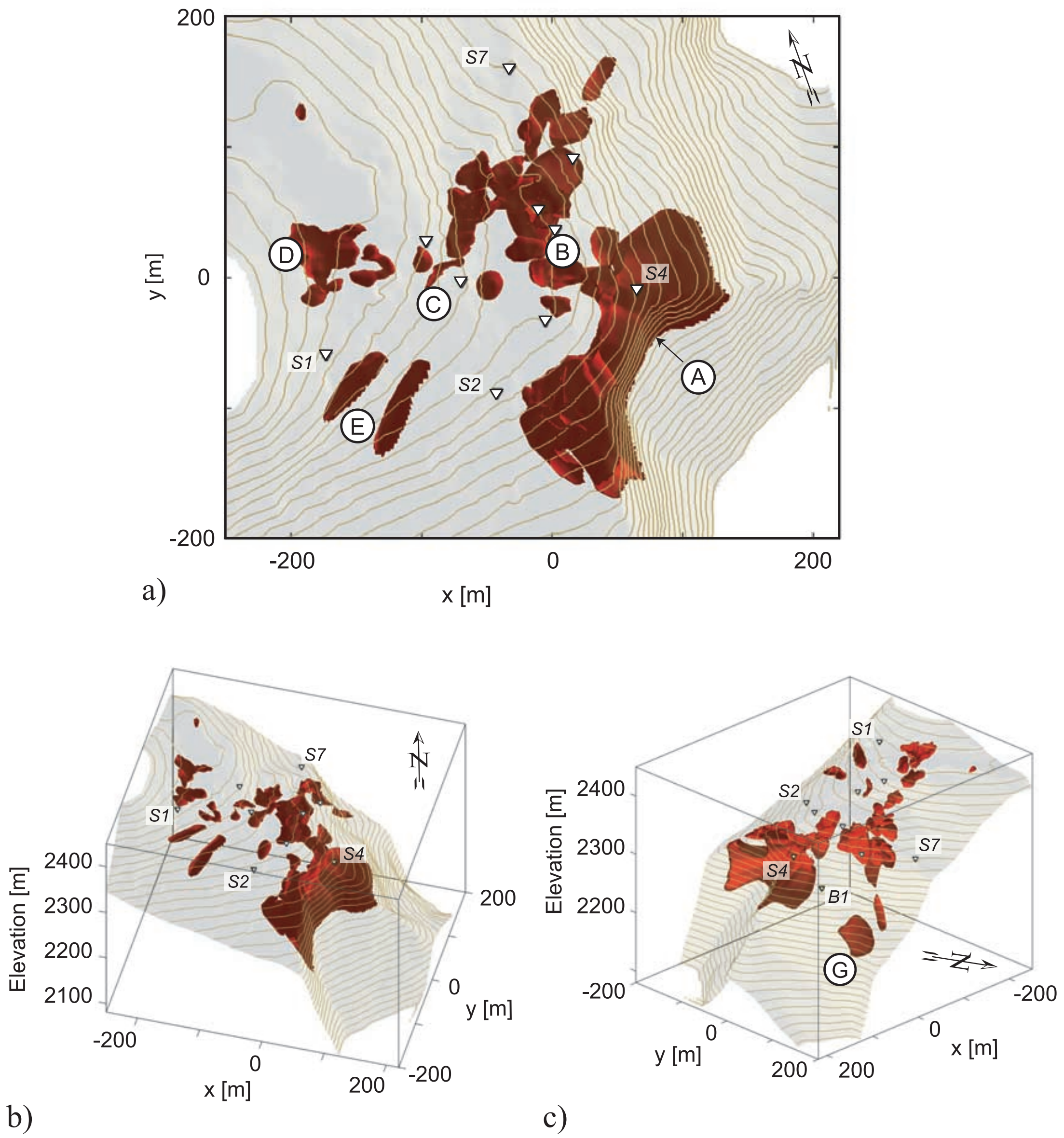

Figure 15. Map and two perspective views of microseismogenic and aseismic zones. The opaque volumes have uniform cumulative hypocenter PDF values $>3.2 \times 10^{-5}$, whereas the transparent regions have uniform values $<3.2 \times 10^{-5}$. Shaded surface and contours represent topography. Letters A–E and G identify features discussed in the text.

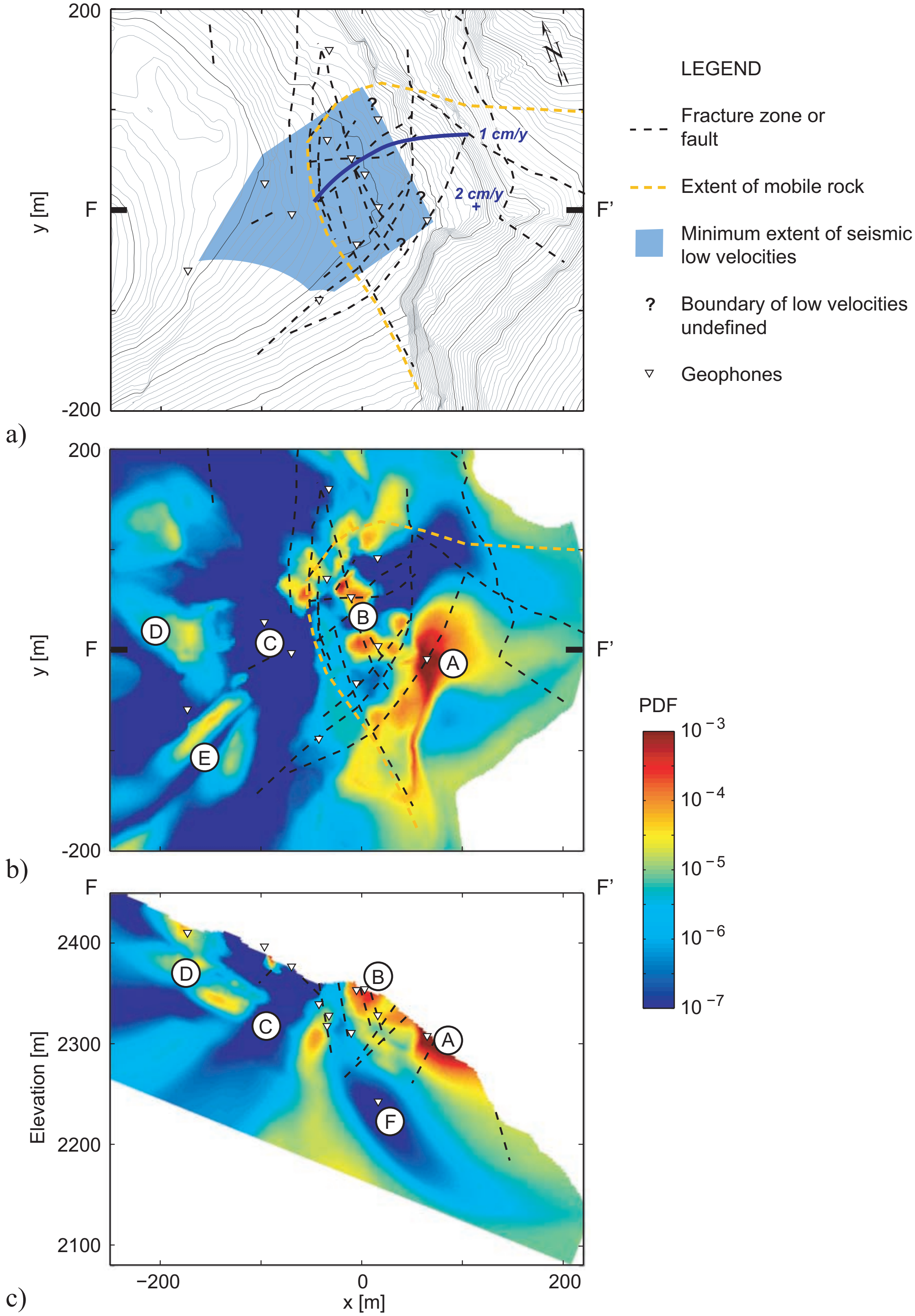

200
-200
y [m]
F
F'
1 cm/y
2 cm/y
?
LEGEND
Fracture zone or fault
Extent of mobile rock
Minimum extent of seismic low velocities
?
Boundary of low velocities undefined
Geophones
a)
A
B
C
D
E
b)
PDF
10^{-3}
10^{-4}
10^{-5}
10^{-6}
10^{-7}
Elevation [m]
2400
2300
2200
2100
F
c)
−200
0
x [m]

Figure 16

tive views of Figure 15, volumes in which the cumulative PDF values are uniformly $> 3.2 \times 10^{-5}$ are opaque and those in which the PDF values are uniformly $< 3.2 \times 10^{-5}$ are transparent (the 3.2×10^{-5} value was found empirically to separate the microseismogenic and aseismic regions). Such diagrams represent well our knowledge of microseismic activity at the site. They provide a robust means of identifying and mapping microseismogenic and aseismic zones.

[48] Figure 16a brings together information on the topography, fracture zones/faults, geodetically determined movements of the unstable mountain slope, and the minimum lateral extent of the anomalously low-velocity crystalline rocks, whereas Figures 16b and 16c show the fracture zones/faults projected on to the PDF slice and cross section of Figures 13d and 13f. The orange dashed line in Figure 16a delineates the boundary of the mobile section of the mountain slope, with the highest rates of displacement occurring south of the blue line [*Jaboyedoff et al.*, 2004]. The displacements are concentrated across major fracture zones/faults with opening rates of 0.001–0.003 m/yr [*Willenberg*, 2004].

[49] In the following, we describe the principal characteristics of the microseismogenic and aseismic features A to G and review information relevant to defining the boundaries of the unstable section of the mountain slope.

9.1. Microseismogenic Zones (A, B, D, E, and G)

[50] The highest levels of microseismic activity are observed within microseismogenic zone A near and beneath the rockslide scarp (Figures 15 and 16). This large zone of enhanced cumulative hypocenter PDF values is approximately 200 m long, 30–100 m wide, and 20–60 m thick. High PDF values extend to the outer limits of the rock mass, such that the southeastern boundary of zone A coincides with the scarp face. Since zone A is mostly outside the microseismic network and the well-resolved part of the extended 3-D velocity model, its internal features and outer boundaries are poorly constrained. Consequently, the microseismicity may not be as widely distributed as suggested by the cumulative hypocenter PDF. Nevertheless, it is significant that a major fracture zone/fault extends the length of zone A (Figures 16b and 16c; see also the linear feature adjacent to geophone S4 in Figure 1c) and that the highest mountain slope displacement rate (2 cm/yr) is recorded within its boundaries (blue cross in Figure 16a). Microearthquakes likely occur along the major fracture zone/fault and on the numerous smaller discontinuities that cause this segment of mountain slope to be highly fractured and craggy (Figure 1c). Considering the paucity of geodetic reflectors in this area, it is possible that most rocks within zone A are moving relatively rapidly southeastward.

[51] Microseismogenic zone B is defined by a number of small to moderately large volumes of high PDF values that occur within the region most affected by major fracture zones/faults (Figures 15 and 16). Although the hypocenters are situated within the boundaries of the network and well-resolved part of the extended 3-D velocity model and are therefore relatively well determined, the location uncertainties and the dense distribution of major discontinuities in this region preclude us from confidently assigning individual microearthquakes to specific fracture zones/faults. However, the close proximity of enhanced PDF values to the fracture zones/faults (Figures 16b and 16c) suggests that the latter are microseismically active. High PDF values along the eastern part of the northern boundary of zone B do not coincide with any known major discontinuity. We note that zone B is characterized by very low seismic velocities that are generally diagnostic of low-quality rock (compare Figures 16a and 16b) [*Heincke et al.*, 2006b].

[52] The scattered volumes of enhanced PDF values that comprise microseismogenic zones D and E are situated near or beyond the boundaries of the microseismic network. As a result, their geometries and locations are poorly constrained. Moreover, they are remote from any mapped fracture zones/faults. Microseismogenic zone D appears to extend from a small terrace above the focus of contemporary surface displacements to approximately 50 m depth. Microearthquakes in zones D and E are evidence for low levels of instability far from the rockslide scarp.

[53] Microseismogenic zone G (only shown on Figure 15c) seems to be situated close to the base of our velocity model, approximately 200 m below the surface. We judge this to be a minimum depth estimate; minor microseismicity may extend deeper in the mountain.

9.2. Aseismic Zones (C and F)

[54] The largely aseismic zone C separates microseismogenic zones A and B from microseismogenic zones D and E. Considering that a large portion of this zone lies within the boundaries of the microseismic network and well-resolved part of the extended 3-D velocity model, the very low cumulative hypocenter PDF values are judged to be reliable. Seismic quiescence may be a consequence of aseismic creep or negligible movements. The lack of major fracture zones, faults, and lineaments throughout this zone is consistent with the latter explanation, but the very low-velocity rocks enclosed by zone C (compare Figures 16a and 16b) must surely be the result of relatively recent movements.

[55] Aseismic zone F immediately below seismic zones A and B was unexpected. It encompassed the lower part of borehole SB120, along which there were many significant fractures and recently measured displacements [*Willenberg*, 2004; *Spillmann et al.*, 2007]. Clearly, these displacements either occurred aseismically or they only generated very small events not detected by a sufficient number of network geophones. A detailed analysis of geophone B1 (located within zone F near the base of SB120) recordings was not

Figure 16. (a) Map showing topography, traces of fracture zones and faults projected to 15 m depth below the surface, minimum extent of unusually low P wave velocities based on refraction tomography, and estimated extent of mobile rock. The rock slope south of the dark blue line is moving southwestward at ≥ 1 cm/yr. The point marked by the blue plus is moving at 2 cm/yr [after *Jaboyedoff et al.*, 2004]. (b) and (c) Undulating section and cross section through the summed PDF volume (reproduced from Figures 13d and 13f) showing fracture zones and faults projected to 15 m depth. Letters A–F identify features discussed in the text.

helpful in distinguishing between these two possibilities, primarily because the data were contaminated with high levels of noise (see Figures 10a and 10c). The source of this noise is unknown.

9.3. Extent of the Unstable Slope

[56] There is a general correspondence between the geodetically determined boundaries of mobile rock and the near-surface borders of microseismogenic zones A and B (Figure 16b), and borehole georadar reflection data demonstrate that fracture zones/faults along the northern and western boundaries of mobile rock (Figure 16b) are important structures that extend at least 50–75 m beneath the surface [*Spillmann et al.*, 2007]. Furthermore, horizontally traveling seismic waves are abruptly truncated at the western boundary (see the seismic section in Figure 5b of *Heincke et al.* [2006b]). In summary, information supplied by the geodetic, georadar, seismic refraction and microseismic investigations is consistent with the lateral extent of mobile rock delineated in Figures 16a and 16b. Moreover, the measured displacements near the base of borehole SB120, the deep-penetrating nature of the fracture zones/faults, and the thicknesses of the microseismogenic zones (Figures 15 and 16c) are compatible with the mobile rock mass having a minimum depth extent of 50–120 m.

[57] Results of the 3-D tomographic seismic refraction survey indicate the presence of low-quality rock beneath a considerable part of the Randa test site [*Heincke et al.*, 2006b]. The section of mountain slope that eventually collapses may well include the large volume of low-velocity crystalline rock that continues >100 m to the west of the mobile rock mass.

9.4. Microseismicity and the Presence of Water

[58] Water under high pressure probably played a role in triggering the 1991 rockslides [*Schindler et al.*, 1993; *Sartori et al.*, 2003]. Accordingly, it is reasonable to ask if water is currently influencing the microseismicity at the Randa test site. Two observations suggest that this is not happening. The top >40 m of all three moderately deep boreholes are usually dry, and we see no convincing correlation between increased microseismicity and high-precipitation rates, unusual accumulations of snow, or periods of rapid snow melting (Figure 17).

10. Discussion and Conclusions

[59] We have completed a pilot microseismicity study of the unstable mountain slope immediately above the huge Randa rockslide scarp in the Swiss Alps. Our microseismic network of 12 three-component geophones placed in shallow and moderately deep holes was distributed across $\sim$60,000 m^2 of rugged terrain. Over a period of 31 months, the network recorded signals from 66,409 events, of which only $\sim$0.3% originated from mountain slope microearthquakes. The majority of microearthquakes had magnitudes in the -2.0 to -0.5 range.

[60] In an earlier phase of our studies, the *P* wave velocities of the mountain slope crystalline rocks were discovered to be extremely heterogeneous [*Heincke et al.*, 2006b]. Inversion of a comprehensive 3-D tomographic seismic refraction data set had revealed the presence of voluminous highly fractured and faulted rocks with very low velocities (<1.5 km/s) juxtaposed against rocks with more normal velocities (>3.8 km/s). To determine reliable hypocenter parameters, it was essential to include the effects of these large velocity variations in the earthquake location process. In a first step toward this goal, we derived an extended 3-D velocity model from the tomographic seismic refraction data set.

[61] In addition to incorporating detailed 3-D velocity information in the hypocenter estimation procedure, it was necessary for us to account for relatively large inaccuracies and/or a shortage of first-arrival picks for some microearthquakes, no reliable *S* wave picks, and the occurrence of numerous microearthquakes outside the microseismic network. Accordingly, traditional approaches [*Lee and Stewart*, 1981] were judged to be unsuitable for locating earthquakes at the Randa study site. By comparison, *Lomax et al.*'s [2000] realization of *Tarantola and Vallete*'s [1982] nonlinear probabilistic location technique allowed us to address all of the critical issues in an efficient and satisfactory manner.

[62] A number of well-located shots provided us with information to calibrate the microseismic network. The nonlinear probabilistic location code was then used to compute hypocenter parameter estimates from the station-corrected first-arrival times. For each microearthquake, we obtained a probability density function that included all plausible hypocenter parameter solutions and complete information on the uncertainties of each parameter. We presented the microseismicity pattern in two formats: (1) a cumulative hypocenter PDF comprising the sum of all individual hypocenter PDFs and (2) the distribution of maximum likelihood locations.

[63] By combining the results of our microseismicity study with information supplied by earlier geological, geodetic, geotechnical, and geophysical investigations, we can summarize the key physical characteristics of the Randa study site as follows:

[64] 1. Extensive regions of the mountain slope are highly fractured and faulted. As a consequence, seismic velocities are extremely heterogeneous and attenuation of the seismic energy is substantial, especially for the high-frequency components; the frequency content of most seismic recordings is limited to 5–100 Hz.

[65] 2. Microseismicity is concentrated in two main zones, one that follows the rockslide scarp and one that coincides with the highest density of fracture zones/faults.

[66] 3. Most microearthquakes occur within 50–100 m of the surface. Considering the generally high attenuation of the seismic energy, it is possible that we do not record or recognize arrivals from deeper events.

[67] 4. The shallow boundaries of the two principal microseismogenic zones correspond closely to the boundaries of slow moving rock defined by geodetic observations. Major fracture zones/faults along these boundaries can be traced to 50–75 m depth on borehole georadar reflection sections. At least one of the boundary fracture zones/faults is a partial barrier to horizontally traveling seismic waves.

[68] 5. A large portion of the slow moving crystalline rock mass and adjacent region to the west is distinguished by exceptionally low seismic velocities. These low velocities are diagnostic of low-quality rock. It is possible that the

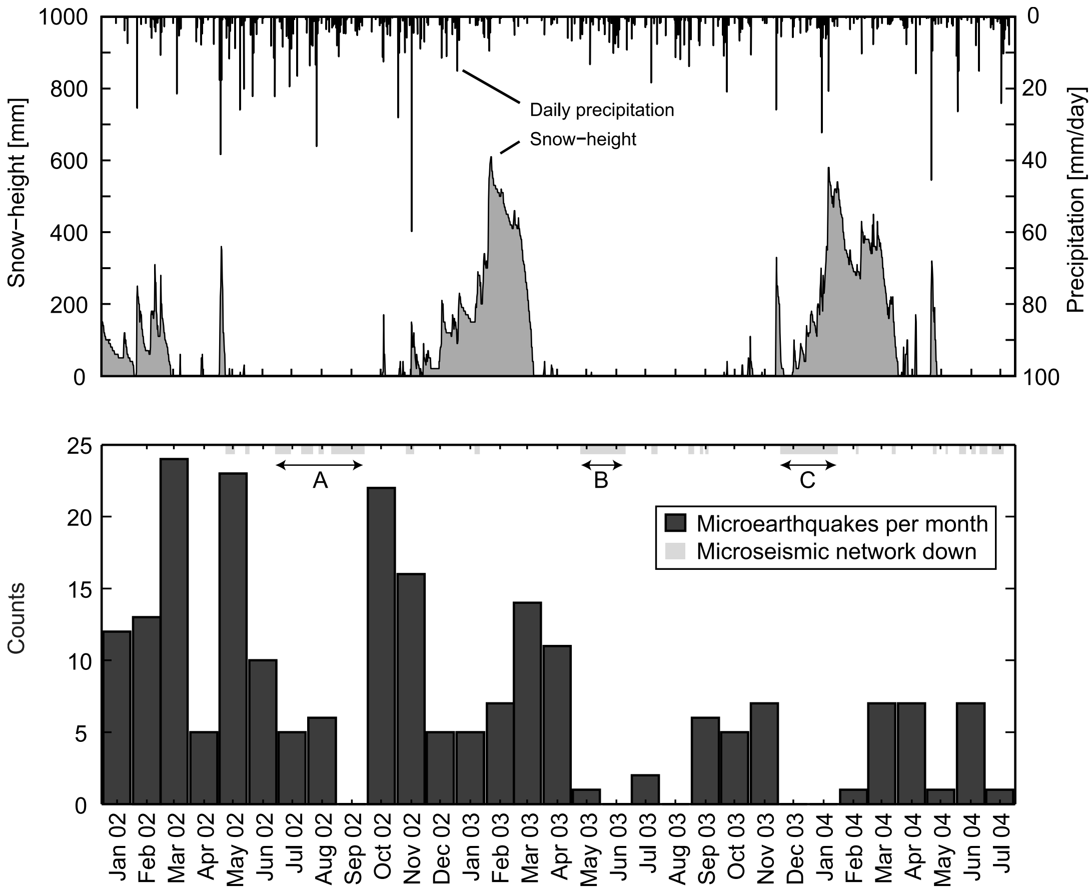

Figure 17. Temporal variations of microseismicity, precipitation, and snow accumulation and melting. During three extensive periods, the microseismic network was either being used for other purposes (A, tomographic seismic refraction survey) or was not operating (B, problems with the on-site field PC; C, problems with the on-site field PC and valley PC).

entire block of low-quality rock will be involved in the eventual next phase of mountain slope collapse.

[69] 6. There are no obvious seasonal variations of microseismicity.

[70] To improve further our understanding of instability processes at the Randa study site, we need to identify the specific fracture zones/faults that are microseismically active and determine microearthquake fault plane mechanisms. These goals can only be achieved by increasing the density of geophones near the potentially seismogenic structures, while at the same time enlarging the network aperture with geophones on the rockslide scarp. The improved geophone density would provide additional recordings rich in the higher frequencies necessary for more accurate first-arrival time determinations and waveform analyses. Although placing geophones on the rockslide scarp would require the assistance of qualified mountaineers and may be dangerous, information supplied by these sensors would improve enormously the location accuracy of most microearthquakes.

[71] We encountered many problems and challenges at the Randa study site, including hazardous and logistically difficult operating conditions, limited aperture of the microseismic network, not enough geophones, strong sources of electrical noise, highly heterogeneous seismic velocities, and high levels of seismic wave attenuation. These difficulties are likely to be characteristic of other microseismic investigations of unstable mountain slopes. As examples, unusually low seismic velocities have already been detected in mountain slope crystalline rocks of the Tien Shan Range [*Havenith et al.*, 2002], French Alps [*Meric et al.*, 2005], and Norwegian Fjords (L. H. Blikra, personal communication, 2005). Our sensitivity tests demonstrate the importance of the velocity model in the earthquake location process; an inaccurate velocity model may result in highly erroneous hypocenter parameters, especially for events near or beyond the microseismic network boundaries.

Appendix A: Semiautomatic Seismic Event Classification

[72] A major effort was required to classify the 66,409 events recorded by the Randa microseismic system. On the basis of a manual analysis of roughly 9000 event files, we designed and implemented a semiautomatic two-step procedure that allowed the entire data set to be classified in an efficient manner (steps I and II in Figure A1). We then studied manually the <7% of event files that potentially contained events of interest (step III in Figure A1).

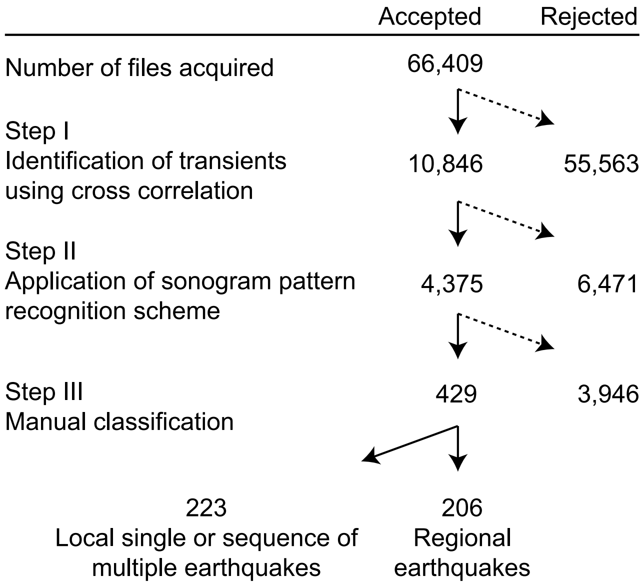

Figure A1. Simple flowchart showing how the various filtering steps result in the recognition of 223 local single and sequences of multiple microearthquakes and 206 regional earthquakes.

A1. Step I: Identification of Impulsive Transients

[73] It was obvious early in our analysis that the vast majority of recorded events were transients. Although they appeared to be relatively uniform spike-like features on standard plots (Figures 4 and A2a), they were seen to have quite complicated waveforms that varied somewhat from channel to channel in expanded time plots (Figure A2b). We considered their very short durations and near simultaneous occurrence on all channels to be diagnostic of electrical noise. They were probably caused by atmospheric electrical discharges and other electrical disturbances associated with the resistive environment of the high mountain and the long recording cables. The strongest signals were recorded on channels connected to the longest cables and essentially the same effects were observed on another seismic instrument (MARS 88) used for testing.

[74] Since the effects of the transients could not be easily eliminated in the field, they were identified and discarded during processing. From M three-component recordings of an event, where M equals 12 the number of stations at Randa, the three-component recordings from the station with the highest signal levels were defined to be the master traces. After dividing all traces into N sections of 500 ms length, with 50% overlap between adjacent sections, unbiased covariance functions between the master trace sections and all other trace sections were computed. This process yielded two matrices: $S(i, j)$ and $L(i, j)$, where $\mathbf{S}$ contained the maxima of the unbiased covariance functions, $\mathbf{L}$ contained the lags of the maxima, and $i = 1 \ldots N$, $j = 1 \ldots 3(M - 1)$. In the next step, the semiautomatic procedure determined i and j at the maximum value of $\mathbf{S}$ $[S(i_{\max}, j_{\max}) = \max(\mathbf{S})]$ and the median value of the $i_{\max}$ row of $\mathbf{L}$ $[\tau = \mathrm{median}(\mathbf{L}(i_{\max}, j))]$. For seismic events and uncorrelated noise, τ was relatively large, whereas for transients it was very small (Figure A2b). A threshold of $\tau \leq 2$ ms was found to be appropriate for identifying the vast majority of transients generated by electrical noise. An

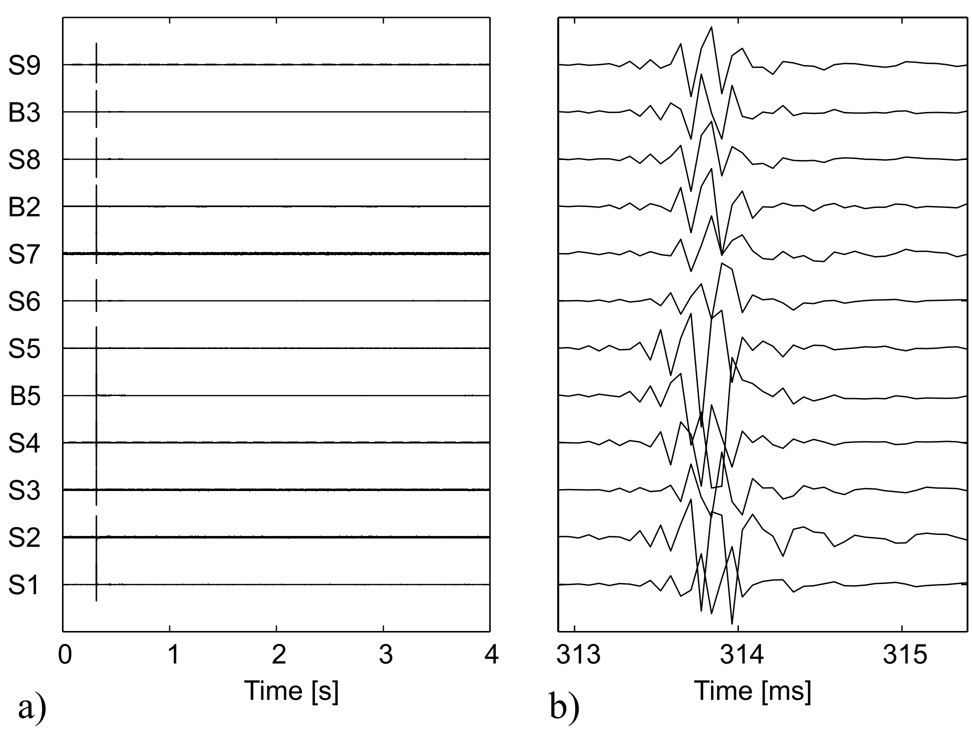

Figure A2. Vertical component seismograms showing the nearly simultaneous occurrence of a transient on all traces. (a) Timescale as for Figure 4. (b) Expanded timescale (note that these seismograms were recorded using a sampling rate of 0.0625 ms). Traces have been normalized to make the maximum positive amplitude on all traces equal.

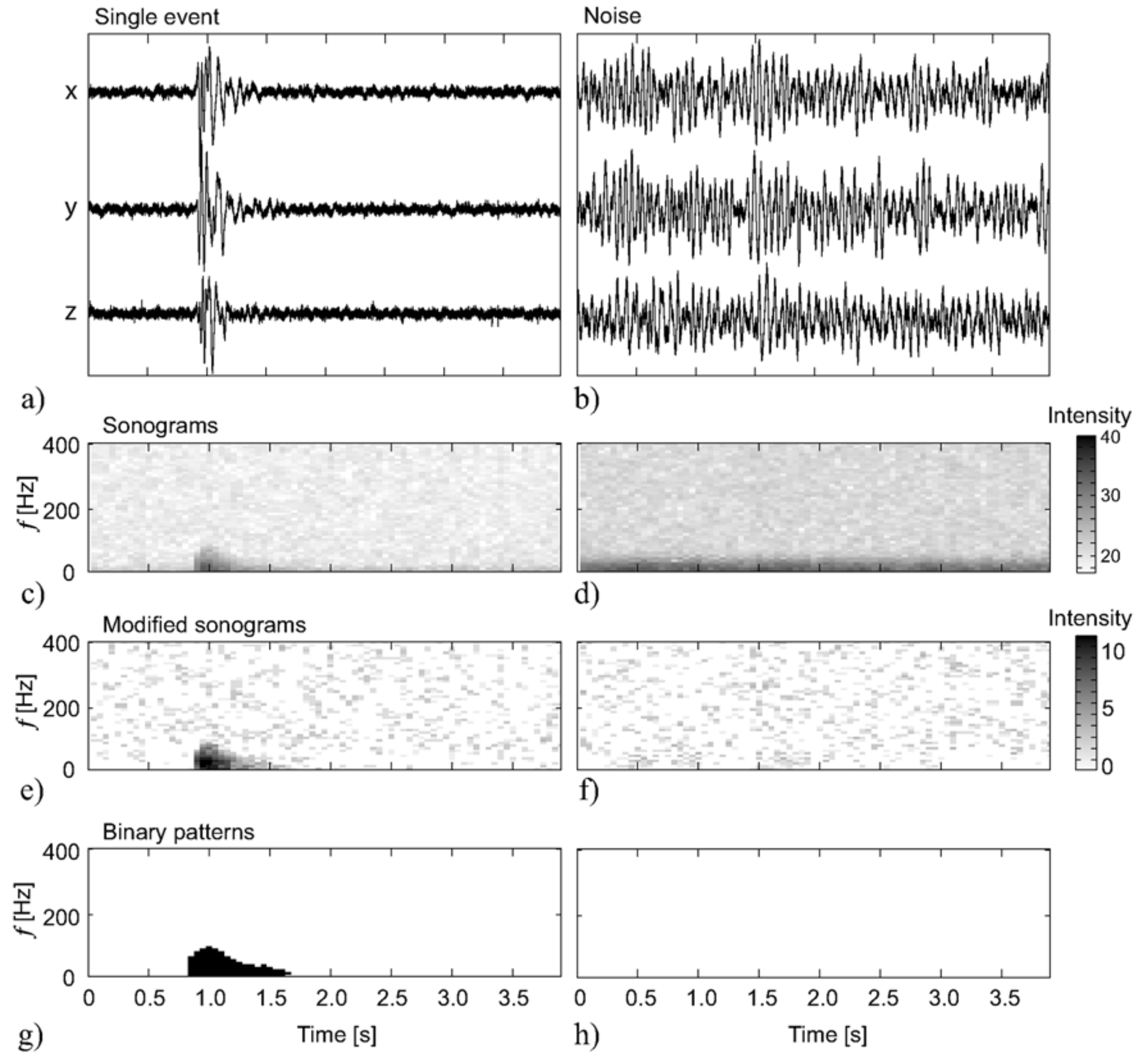

Figure A3. Example of the sonogram (spectrograms or running spectra) processing scheme applied to three-component seismograms of (left) a typical microearthquake and (right) noise. (a) and (b) Seismograms. (c) and (d) Sonogram stacks. (e) and (f) Sonogram stacks after noise reduction. (g) and (h) Binary patterns derived from the sonograms. Note the absence of signal in Figure A3h for the noise recording in Figure A3b. See text for details.

event file containing both a transient and a seismic signal was discarded if the amplitude of the transient was substantially larger than that of the seismic signal. Application of this algorithm yielded 55,563 noise transients (i.e., ~84% of all events; Figure A1). Results of applying this algorithm to the manually assessed subset of 9000 events suggest that less than 2% of the seismic events would have been erroneously classified as transients.

A2. Step II: Sonogram Pattern Recognition Scheme

[75] Once most of the transients were removed, it was necessary to distinguish between files that contained potentially interesting seismic events and those that only contained noise or signals with low coherency. To meet this objective, we employed a modified version of *Joswig*'s [1995] sonogram (spectrogram or running spectra) pattern recognition scheme, in which the time variation of a recording's frequency content was used as a discriminant. The results of applying this procedure to typical three-component recordings of a rock slope microearthquake and noise are presented in Figure A3. To compute the sonograms presented in Figures A3c and A3d, we (1) divided each trace of a three-component recording (Figures A3a and A3b) into 100-ms-long sections with 50% overlap between adjacent sections; (2) tapered the ends of each section using a cosine function and computed the energy spectrum; (3) summed the spectra of the respective three components and took the logarithm (basis 2) of the sum; and (4) plotted the running $\log_2$ spectra on a time-versus-frequency graph using a gray scale representation for the intensity levels.

[76] To highlight better the signal due to the seismic event, it was necessary to define a model for the background noise. Following *Joswig* [1995], we assumed that noise in the frequency domain could be adequately defined by a lognormal distribution, which translated to a Gaussian distribution in $\log_2$ space. We then only accepted values of the sonogram that exceeded an amplitude threshold based on the noise model (Figures A3e and A3f; see equations (3)

to (7) in *Joswig* [1995]). Although the human eye could distinguish seismic signal from background noise in the modified sonograms of Figures A3e and A3f, some extra processing was required for it to be identified as meaningful signal using an automated computer-based approach. This was achieved by setting to 0 all intensity values ≤ 3 in the modified sonograms, setting to 1 all intensity values > 3, and then applying an image morphology process that flattened and preserved essential shape characteristics while removing protuberances and noise [*Pratt*, 2001; *Heincke et al.*, 2006a]. The final binary patterns are shown in Figures A3g and A3h.

[77] Since we were primarily interested in microearthquakes that could be located, the final step of our semiautomatic scheme involved identifying events that were recorded on multiple channels. Tests on the subset of 9000 events demonstrated that this could be achieved by demanding that at least 10 of the 12 binary patterns significantly overlapped. Indeed, all 12 binary patterns overlapped for microearthquakes that generated recordings with moderately high signal-to-noise ratios. After applying this process, 6471 files containing noise and low-coherency events were discarded (Figure A1).

A3. Step III: Manual Classification

[78] A manual inspection of the remaining 4375 event files was the final step in our classification procedure. Based mainly on their frequency contents and coda lengths, we identified 223 single microearthquakes and sequences of multiple microearthquakes that were probably generated within the unstable mountain slope and 206 small regional earthquakes (Figure A1). The remaining 3961 files contained relatively low-frequency, low-amplitude emergent signals that were probably generated by distant earthquakes and explosions and low-quality signals from which we could not determine event locations.

[79] **Acknowledgments.** We thank Christoph Bärlocher and Beat Rinderknecht for their considerable technical assistance in establishing and operating the microseismic network; numerous people for field assistance; Anthony Lomax for providing the NonLinLoc software package and valuable discussion; Heinrich Horstmeyer for assistance and advise on the ETH data processing system; Nicholas Deichmann, Simon Loew, Keith Evans, and Erik Eberhardt for their cooperation in this interdisciplinary project; Jean Daniel-Rouiller and colleagues from CREALP (Research Centre on Alpine Environment, Switzerland) for supplying the digital terrain model and geodetic survey data; the local authorities of Randa for providing logistical support; and the journal editors and reviewers for their constructive comments on the first draft of this manuscript. This project was funded by the Swiss National Science Foundation.

References

Aki, K., and P. G. Richards (1980), *Quantitative Seismology*, 1st ed., 932 pp., W. H. Freeman, New York.

Amitrano, D., J. R. Grasso, and G. Senfaute (2005), Seismic precursory patterns before a cliff collapse and critical point phenomena, *Geophys. Res. Lett.*, *32*, L08314, doi:10.1029/2004GL022270.

Antonello, G., N. Casagli, P. Farina, D. Leva, G. Nico, A. J. Sieber, and D. Tarchi (2004), Ground-based SAR interferometry for monitoring mass movements, *Landslides*, *1*, 21–28.

Brückl, E., and J. Brückl (2006), Geophysical models of the Lesachriegel and Gradenbach deep-seated mass-movements (Schober range, Austria), *Eng. Geol.*, *83*, 254–272.

Brückl, E., and M. Parotidis (2005), Prediction of slope instabilities due to deep-seated gravitational creep, *Nat. Hazards Earth Syst. Sci.*, *5*, 155–172.

Bruno, F., and F. Marillier (2000), Test of high-resolution seismic reflection and other geophysical techniques on the Boup landslide in the Swiss Alps, *Surv. Geophys.*, *21*, 335–350.

Bulmer, M. H., D. N. Petley, W. Murphy, and F. Mantovani (2006), Detecting slope deformation using two-pass differential interferometry: Implications for landslide studies on Earth and other planetary bodies, *J. Geophys. Res.*, *111*, E06S16, doi:10.1029/2005JE002593.

Burgmann, R., G. Hilley, A. Ferretti, and F. Novali (2006), Resolving vertical tectonics in the San Francisco Bay Area from permanent scatterer InSAR and GPS analysis, *Geology*, *34*, 221–224.

Catani, F., P. Farina, S. Moretti, G. Nico, and T. Strozzi (2005), On the application of SAR interferometry to geomorphological studies: Estimation of landform attributes and mass movements, *Geomorphology*, *66*, 119–131.

Cummings, D. (2000), Transient electromagnetic survey of a landslide and fault, Santa Susanna Mountains, southern California, *Environ. Eng. Geosci.*, *6*, 247–254.

De Natale, G., P. Capuano, C. Troise, and A. Zollo (1998), Seismicity at Somma-Vesuvius and its implications for the 3D tomography of the volcano, *J. Volcanol. Geotherm. Res.*, *82*, 175–197.

Dunnicliff, J. (1988), *Geotechnical Instrumentation for Monitoring Field Performance*, 577 pp., John Wiley, New York.

Dussauge-Peisser, C., M. Wathelet, D. Jongmans, D. Hantz, B. Couturier, and M. Sintes (2003), Investigation of a fractured limestone cliff (Chartreuse Massif, France) using seismic tomography and ground-penetrating radar, *Near Surf. Geophys.*, *1*, 161–170.

Eberhardt, E., H. Willenberg, S. Loew, and H. R. Maurer (2001), Active rockslides in Switzerland—Understanding mechanisms and processes, in *International Conference on Landslides: Causes, Impacts and Countermeasures*, edited by M. Kühne et al., pp. 25–34, Verlag Glückauf, Davos, Switzerland.

Eberhardt, E., D. Stead, and J. S. Coggan (2004a), Numerical analysis of initiation and progressive failure in natural rock slopes: The 1991 Randa rockslide, *Int. J. Rock Mech. Min. Sci.*, *41*, 69–87.

Eberhardt, E., T. Spillmann, H. R. Maurer, H. Willenberg, S. Loew, and D. Stead (2004b), The Randa Rockslide Laboratory: Establishing brittle and ductile instability mechanisms using numerical modelling and microseismicity, in *Proceedings of the 9th International Symposium of Landslides*, *Rio de Janeiro, June 28–July 2*, pp. 481–487, A. A. Balkema, Brookfield, Vt.

Evans, K. F., H. Moriya, H. Niitsuma, R. H. Jones, W. S. Phillips, A. Genter, J. Sausse, R. Jung, and R. Baria (2005), Microseismicity and permeability enhancement of hydrogeologic structures during massive fluid injections into granite at 3 km depth at the Soultz HDR site, *Geophys. J. Int.*, *160*, 388–412.

Flinn, E. A. (1965), Signal analysis using rectilinearity and direction of particle motion, *Proc. IEEE*, *53*, 1874–1876.

Geertsema, M., J. J. Clague, J. W. Schwab, and S. G. Evans (2006), An overview of recent large catastrophic landslides in northern British Columbia, Canada, *Eng. Geol.*, *83*, 120–143.

Glade, T., M. Anderson, and M. J. Crozier (2005), *Landslide Hazard and Risk*, John Wiley, New York.

Glenn, N. F., D. R. Streutker, D. J. Chadwick, G. D. Thackray, and S. J. Dorsch (2006), Analysis of LiDAR-derived topographic information for characterizing and differentiating landslide morphology and activity, *Geomorphology*, *73*, 131–148.

Godio, A., C. Strobbia, and G. De Bacco (2006), Geophysical characterisation of a rockslide in an alpine region, *Eng. Geol.*, *83*, 273–286.

Green, A. G., H. R. Maurer, T. Spillmann, B. Heincke, and H. Willenberg (2006), High-resolution geophysical techniques for improving hazard assessments of unstable rock slopes, *Leading Edge*, *25*, 311–316.

Hack, R. (2000), Geophysics for slope stability, *Surv. Geophys.*, *21*, 423–448.

Hanks, T. C., and H. Kanamori (1979), Moment magnitude scale, *J. Geophys. Res.*, *84*, 2348–2350.

Havenith, H.-B., D. Jongmans, K. Abdrakhmatov, P. Trefois, D. Delvaux, and I. A. Torgoev (2000), Geophysical investigations of seismically induced surface effects: Case study of a landslide in the Suusamyr valley, Kyrgyzstan, *Surv. Geophys.*, *21*, 351–370.

Havenith, H. B., D. Jongmans, E. Faccioli, K. Abdrakhmatov, and P. Y. Bard (2002), Site effect analysis around the seismically induced Ananevo, Rockslide, Kyrgyzstan, *Bull. Seismol. Soc. Am.*, *92*, 3190–3209.

Heincke, B., A. G. Green, J. van der Kruk, and H. Horstmeyer (2005), Acquisition and processing strategies for 3D georadar surveying a region characterized by rugged topography, *Geophysics*, *70*, K53–K61.

Heincke, B., A. G. Green, J. van der Kruk, and H. Willenberg (2006a), Semblance-based topographic migration (SBTM): A method for identifying fracture zones in 3-D georadar data, *Near Surf. Geophys.*, *4*, 79–88.

Heincke, B., H. Maurer, A. G. Green, H. Willenberg, T. Spillmann, and L. Burlini (2006b), Characterizing an unstable mountain slope using shallow 2D and 3D seismic tomography, *Geophysics*, *71*, B241–B256.

Hilley, G. E., R. Burgmann, A. Ferretti, F. Novali, and F. Rocca (2004), Dynamics of slow-moving landslides from permanent scatterer analysis, *Science*, *304*, 1952–1955.
Husen, S., and R. B. Smith (2004), Probabilistic earthquake relocation in three-dimensional velocity models for the Yellowstone National Park Region, Wyoming, *Bull. Seismol. Soc. Am.*, *94*, 880–896.
Husen, S., E. Kissling, N. Deichmann, S. Wiemer, D. Giardini, and M. Baer (2003), Probabilistic earthquake location in complex three-dimensional velocity models: Application to Switzerland, *J. Geophys. Res.*, *108*(B2), 2077, doi:10.1029/2002JB001778.
Iannacchione, A. T., G. S. Esterhuizen, T. S. Bajpayee, P. L. Swanson, and M. C. Chapman (2005), Characteristics of mining-induced seismicity associated with roof falls and roof caving events, in *Proceedings of the 40th U.S. Rock Mechanics Symposium*, edited by G. Chen et al., pp. 1–10, Am. Rock Mech. Assoc., Anchorage, Alaska.
Jaboyedoff, M., P. Ornstein, and J.-D. Rouiller (2004), Design of a geodetic database and associated tools for monitoring rock-slope movements: The example of the top of Randa rockfall scarp, *Nat. Hazards Earth Syst. Sci.*, *204*, 187–196.
Jongmans, D., P. Hemroulle, F. Demanet, F. Renardy, and Y. Vanbrabant (2000), Application of 2-D electrical and seismic tomography techniques for investigating landslides, *Eur. J. Environ. Eng. Geophys.*, *5*, 75–89.
Joswig, M. (1995), Automated classification of local earthquake data in the BUG small array, *Geophys. J. Int.*, *120*, 262–286.
Julian, B. R., A. D. Miller, and G. R. Foulger (1998), Non-double-couple earthquakes 1. Theory, *Rev. Geophys.*, *36*, 525–549.
Kilburn, C. R. J., and D. N. Petley (2003), Forecasting giant, catastrophic slope collapse: Lessons from Vajont, northern Italy, *Geomorphology*, *54*, 21–32.
Lee, W. H. K., and S. W. Stewart (1981), *Principles and Applications of Microearthquake Networks*, 293 pp., Academic, New York.
Lippitsch, R., R. White, and H. Soosalu (2005), Precise hypocenter relocation of microearthquakes in a high-temperature geothermal field: The Torfajökull central volcano, Iceland, *Geophys. J. Int.*, *160*, 370–387.
Lomax, A. (2005), A reanalysis of the hypocentral location and related observations for the great 1906 California earthquake, *Bull. Seismol. Soc. Am.*, *95*, 861–877.
Lomax, A., J. Virieux, P. Volant, and C. Thierry-Berge (2000), Probabilistic earthquake location in 3D and layered models, in *Advances in Seismic Events Location*, edited by C. H. Thurber and N. R. Rabinowitz, pp. 101–134, Kluwer Acad., Norwell, Mass.
Lomax, A., A. Zollo, P. Capuano, and J. Virieux (2001), Precise, absolute earthquake location under Somma-Vesuvius volcano using a new three-dimensional velocity model, *Geophys. J. Int.*, *146*, 313–331.
Malin, P. E., S. N. Blakeslee, M. G. Alvarez, and A. J. Martin (1989), Microearthquake imaging of the Parkfield asperity, *Science*, *244*, 557–559.
Maurer, H., and U. Kradolfer (1996), Hypocentral parameters and velocity estimation in the western Swiss Alps by simultaneous inversion of P- and S-wave data, *Bull. Seismol. Soc. Am.*, *86*, 32–42.
Mauritsch, H. J., W. Seiberl, R. Arndt, A. Romer, K. Schneiderbauer, and G. P. Sendlhofer (2000), Geophysical investigations of large landslides in the Carnic Region of southern Austria, *Eng. Geol.*, *56*, 373–388.
McCann, D. M., and A. Forster (1990), Reconnaissance geophysical methods in landslide investigations, *Eng. Geol.*, *29*, 59–78.
Menke, W. (1989), *Geophysical Data Analysis: Discrete Inverse Theory*, rev. ed., 290 pp., Academic, San Diego, Calif.
Meric, O., S. Garambois, D. Jongmans, M. Wathelet, J. L. Chatelain, and J. M. Vengeon (2005), Application of geophysical methods for the investigation of the large gravitational mass movement of Sechilienne, France, *Can. Geotech. J.*, *42*, 1105–1115.
Merrien-Soukatchoff, V., C. Clément, G. Senfaute, and Y. Gunzburger (2005), Monitoring of a potential rockfall zone: The case of "Rochers de Valabres" site, in *Proceedings of the International Conference on Landslide Risk Management, Vancouver, 31 May–3 June, 2005* [CD-ROM], Paper C080, 7 pp., edited by O. Hungr et al., A. A. Balkema, Leiden, Germany.
Metternicht, G., L. Hurni, and R. Gogu (2005), Remote sensing of landslides: An analysis of the potential contribution to geo-spatial systems for hazard assessment in mountainous environments, *Remote Sens. Environ.*, *98*, 284–303.
Miller, A. D., G. R. Foulger, and B. R. Julian (1998), Non-double-couple earthquakes: 2. Observations, *Rev. Geophys.*, *36*, 551–568.
Oye, V., and M. Roth (2003), Automated seismic event location for hydrocarbon reservoirs, *Comput. Geosci.*, *29*, 851–863.
Pezzo, E. D., F. Bianco, and G. Saccorotti (2004), Seismic source dynamics at Vesuvius volcano, Italy, *J. Volcanol. Geotherm. Res.*, *133*, 23–39.
Podvin, P., and I. Lecomte (1991), Finite difference computation of traveltimes in very contrasted velocity models: A massively parallel approach and its associated tools, *Geophys. J. Int.*, *105*, 271–284.
Pratt, W. (2001), *Digital Image Processing*, John Wiley, New York.
Presti, D., C. Troise, and G. De Natale (2004), Probabilistic location of seismic sequences in heterogeneous media, *Bull. Seismol. Soc. Am.*, *94*, 2239–2253.
Roth, M., M. Dietrich, L. H. Blikra, and I. Lecomte (2006), Seismic monitoring of the unstable rock slope site at Åknes, Norway, in *19th Annual Symposium on the Application of Geophysics to Engineering and Environmental Problems (SAGEEP)*, edited by J. Gamey, pp. 184–192, Environ. and Eng. Geophys. Soc., Denver, Colo.
Rouse, C., P. Styles, and S. A. Wilson (1991), Microseismic emissions from flowslide-type movements in South Wales, *Eng. Geol.*, *31*, 91–110.
Rutledge, J. T., W. Phillips, and B. K. Schuessler (1998), Reservoir characterization using oil-production-induced microseismicity, Clinton County, Kentucky, *Tectonophysics*, *289*, 129–152.
Sartori, M., F. Baillifard, M. Jaboyedoff, and J.-D. Rouiller (2003), Kinematics of the 1991 Randa rockslides (Valais, Switzerland), *Nat. Hazards Earth Syst. Sci.*, *3*, 423–433.
Schindler, C., Y. Cuénod, T. Eisenlohr, and C.-L. Joris (1993), Die Ereignisse vom 18. April und 9. Mai8 1991 bei Randa (VS): Ein atypischer Bergsturz in Raten, *Eclogae Geol. Helv.*, *86*, 643–665.
Schmutz, M., Y. Albouy, R. Guérin, O. Maquaire, J. Vassal, J.-J. Schott, and M. Descloîtres (2000), Joint electrical and time domain electromagnetism (TDEM) data inversion applied to the Super Sauze earth flow (France), *Surv. Geophys.*, *21*, 371–390.
Schorlemmer, D., and S. Wiemer (2005), Microseismicity data forecast rupture area, *Nature*, *434*, 1086.
Spillmann, T., H. R. Maurer, H. Willenberg, F. E. Evans, B. Heincke, and A. G. Green (2007), Characterization of an unstable rock mass based on borehole logs and diverse borehole radar data, *J. Appl. Geophys.*, *61*, 16–38.
Stead, D., E. Eberhardt, and J. S. Coggan (2006), Developments in the characterization of complex rock slope deformation and failure using numerical modelling techniques, *Eng. Geol.*, *83*, 217–235.
Tarantola, A., and B. Valette (1982), Inverse problems: Quest for information, *J. Geophys.*, *50*, 159–170.
Trifu, C. I., and T. I. Urbancic (1996), Fracture coalescence as a mechanism for earthquakes: Observations based on mining induced microseismicity, *Tectonophysics*, *261*, 193–207.
Vécsey, G., K. Holliger, R. G. Pratt, B. C. Dyer, and A. G. Green (1998), Anisotropic seismic tomography of a potential hot dry rock reservoir before and during induced pressurization, *Geophys. Res. Lett.*, *25*, 1991–1994.
Vilardo, G., G. DeNatale, G. Milano, and U. Coppa (1996), The seismicity of Mt Vesuvius, *Tectonophysics*, *261*, 127–138.
Willenberg, H. (2004), Geologic and kinematic model of a landslide in crystalline rock (Randa, Switzerland), Ph.D. thesis, ETH-Zurich, Zurich.
Willenberg, H., T. Spillmann, E. Eberhardt, K. Evans, S. Loew, and H. R. Maurer (2002), Multidisciplinary monitoring of progressive failure processes in brittle rock slopes: Concepts and system design, in *Landslides: First European Conference on Landslides*, edited by J. Rybár, J. Stemberk and P. Wagner, pp. 477–483, A. A. Balkema, Brookfield, Vt.
Willenberg, H., K. F. Evans, E. Eberhardt, and S. Loew (2003), Monitoring of complex rock slope instabilities: Correction and analysis of inclinometer/extensometer surveys and integration with surface displacement data, in *Sixth International Symposium on Field Measurements in Geomechanics*, edited by F. Myrvoll, pp. 393–400, A. A. Balkema, Brookfield, Vt.

A. G. Green and H. Maurer, Institute of Geophysics, ETH-Zurich, CH-8093 Zurich, Switzerland. (alan@aug.ig.erdw.ethz.ch)
B. Heincke, NGU, Leiv Erikssons vei 39, N-7491 Trondheim, Norway.
S. Husen, Swiss Seismological Service, ETH-Zurich, CH-8093 Zurich, Switzerland.
T. Spillmann, Geothermal Explorers Ltd., Scholossstrasse 3, CH-4133 Pratteln, Switzerland. (tom.spillmann@magnet.ch)
H. Willenberg, Geological Institute, ETH-Zurich, CH-8093 Zurich, Switzerland.